arXiv:astro-ph/9812104v1 4 Dec 1998

The Statistical Approach to Quantifying Galaxy Evolution

Robert J. Brunner[1,2], Andrew J. Connolly[1], and Alexander S. Szalay

{rbrunner,ajc,szalay}@pha.jhu.edu

Department of Physics & Astronomy, The Johns Hopkins University, Baltimore, MD 21218

Received _____; accepted _____

[1]Visiting Astronomer, Kitt Peak National Observatory, National Optical Astronomy Observatories, which is operated by the Association of Universities for Research in Astronomy, Inc. (AURA) under cooperative agreement with the National Science Foundation.

[2]Current Address: rb@astro.caltech.edu, Department of Astronomy, California Institute of Technology, MC 105-24, Pasadena, CA 91125

ABSTRACT

Studies of the distribution and evolution of galaxies are of fundamental importance to modern cosmology; these studies, however, are hampered by the complexity of the competing effects of spectral and density evolution. Constructing a spectroscopic sample that is able to unambiguously disentangle these processes is currently excessively prohibitive due to the observational requirements. This paper extends and applies an alternative approach that relies on statistical estimates for both distance (z) and spectral type to a deep multi-band dataset that was obtained for this exact purpose.

These statistical estimates are extracted directly from the photometric data by capitalizing on the inherent relationships between flux, redshift, and spectral type. These relationships are encapsulated in the empirical photometric redshift relation which we extend to $z \approx 1.2$, with an intrinsic dispersion of $\delta z \sim 0.06$. We also develop realistic estimates for the photometric redshift error for individual objects, and introduce the utilization of the galaxy ensemble as a tool for quantifying both a cosmological parameter and its measured error. We present deep, multi-band, optical number counts as a demonstration of the integrity of our sample. Using the photometric redshift and the corresponding redshift error, we can divide our data into different redshift intervals and spectral types. As an example application, we present the number redshift distribution as a function of spectral type.

Subject headings: cosmology: observations - galaxies: evolution - galaxies: photometry

1. Introduction

With the advent of the Hubble Deep Field (Williams *et al.* 1996), which imaged objects that are approximately 100 times fainter than the limit of ground based spectrographs, deriving redshifts from broadband photometry has undergone a renaissance. However, the utility of deriving galaxy redshifts from photometric data has long been known (Baum 1962, Koo 1985, Loh & Spillar 1986). The majority of the more recently promoted redshift estimation techniques rely on fitting template spectral energy distributions to the observed galaxy magnitudes (Lanzetta *et al.* 1996, Gwyn & Hartwick 1996, Sawicki *et al.* 1996, Mobasher *et al.* 1996). An alternative, empirical, approach was developed by Connolly *et al.* (1995), in which the redshift is estimated directly from the broadband magnitudes. Utilizing photographic data, they were able to estimate a redshift out to $z \sim 0.5$ with a measured dispersion of $\delta z < 0.05$. The uncertainties in that result were dominated by the photometric errors, and simulations indicated that with improved photometry, the dispersion within the relationship could be significantly reduced.

Preliminary results (Brunner *et al.* 1997) from these data indicate that this empirical approach can recover redshifts from broadband magnitudes with a measured intrinsic dispersion of $\delta z \approx 0.02$ to $z \sim 0.4$, which is remarkably close to the asymptotic intrinsic dispersions ($\delta z \approx 0.016$ for $z < 0.4$) that were previously predicted from simulated distributions of galaxy colors. The rest of this paper extends this published analysis to higher redshifts and provides a framework for quantifying galaxy evolution. Specifically, we discuss the observations and data reduction in Section 2. In Section 3 we present the deep, multi-band number counts from this data. The photometric redshift and corresponding error estimates are presented in section 4; and the classification of the data by spectral type data is detailed in Section 5. We present the number redshift distribution in Section 6 as a simple application of the statistical approach. We conclude this paper with a discussion of

the general technique and its applicability.

2. Data

2.1. Photometric Observations

The photometric data presented in this paper are located in the intersection between the *HST* 5096 field and the CFRS 14 hour field (*i.e.* the Groth Strip), covering approximately 0.054 Sq. Degree. All of the photometric data were obtained using the Prime Focus CCD (PFCCD) camera on the Mayall 4 meter telescope at Kitt Peak National Observatory (KPNO). The observations were performed on the nights of March 31 - April 3, 1995, March 18 - 20, 1996, and May 14 - 16, 1996. The PFCCD uses the T2KB CCD, a 2048^2 Tektronix CCD with 24 micron pixel scale, which at $f/2.8$ in the 4 meter results in a scale of $0.47''$/pixel and a field of view of $\approx 16.0' \times 16.0'$. The T2KB has a measured RMS read noise of $4e^-$/pixel (Massey *et al.* 1995), and has a high charge transfer efficiency as well as reasonable throughput in the ultra-violet.

All observations were made through the broadband filters: $U, B, R, \& \ I$, commonly referred to at Kitt Peak as the "Harris Set" (*cf.* Figure 1). These filters were chosen due to their large spectral coverage, and are commonly used in deep, sky limited broadband imaging. The total integration times for each filter are listed along with the corresponding magnitude limits in Table 1.

EDITOR: PLACE TABLE 1 HERE.

EDITOR: PLACE FIGURE 1 HERE.

During the course of the program observations, the standard set of calibration data: bias frames, dark frames, and flat fields, were taken. These data are necessary to both properly remove the instrumental signature from the data, as well as to provide real-time integrity tests for both the CCD and the electronics. Multiple flat field images were taken at both the beginning and end of each night by illuminating a white screen mounted inside the dome. A visual inspection of the illumination pattern uncovered an irregularity which was manifested in the flat field images themselves. This required the construction of illumination correction images during the reduction process. For all of our program data, we utilized a short scan of fifty rows.

One final concern in using the PFCCD on the Mayall 4 meter was maintaining a consistent focus over the image. The focus solution varied throughout the night due to temperature fluctuations, and our adopted solution was to monitor the PSF within our images. The focus value for the current filter was chosen to optimize the PSF at approximately one third of the radial distance outward from the center of the image. Focus offsets that were determined at the beginning of each night were then applied when switching between the different program filters.

2.2. Photometric Data Reduction

The photometric data were reduced in the standard fashion and are extensively detailed elsewhere (Brunner 1997); however, due to the relevance of the accuracy of the photometric measurements, we present a brief overview of the process. The bias pattern, which was very stable, was removed by using a global bias frame, which was constructed by combining all of the acceptable bias frames for a given run. Variations in the bias level were removed using the overscan region for each individual program image. During each run, the dark current was examined and found to be both stable and uniform; and, as a result, we

applied no corrections for dark current in any of our data frames. The small scale pixel to pixel variations were removed using dome flats, and the residual large scale gradients were removed using illumination corrections which were created from smoothed super-sky flat images. A fringe correction image was constructed from the I band sky flat to remove any fringing due to OH line emission.

Cosmic rays (radiation events) were removed both by looking for deviant pixels, and by utilizing a pixel rejection strategy during the image stacking phase. Cosmetic defects were corrected by linearly interpolating over them. Any charge depletions introduced into the images by the CCD electronics were corrected (*cf.* Brunner 1997), reducing any remaining variations to a few tenths of a percent.

Before combining the images, the geometric distortions were mapped using a third order polynomial with cross terms fit to nine reference stars. The images were transformed to the reference image, and stacked using signal-to-noise weighting for each separate run. The final stacked images for each of the three runs were also registered, stacked, and trimmed in a similar manner. The final image section for the deep stacked region is 1641 rows by 1943 columns, or ≈ 0.054 Sq. Degree.

2.3. Photometric Calibration

All photometric calibrations were done using the April 1995 dataset which included published standard star fields (Landolt 1992). Once the calibration frames were reduced, a curve of growth was generated for each standard star in concentric apertures of diameters from $4''$ to $20''$. All standard stars for which the curve of growth converged were used to determine the photometric solution. A linear regression on the published stellar magnitude, the instrumental magnitude, the airmass, and a color term was performed, and the result

translated to a one second standard exposure. We transformed our magnitude system to the AB system (Oke & Gunn, 1983) using published transformations (Fukugita *et al.* 1995).

During the registration and stacking phase of the data reduction, both photometric and non-photometric frames were combined. As a result, the photometric calibration required a direct cross calibration between the stacked image and a photometric calibrated reference image. This cross calibration was done using a large number of high signal to noise reference stars in order to derive the photometric relationship between the two frames. The dispersion in the cross calibration relationship between the stacked and reference frames was a few hundredths in each band, and our overall intrinsic photometric accuracy was better than two percent.

2.4. Source Detection and Photometry

Source detection and photometry were performed using SExtractor version 2.0.8 (Bertin & Arnouts 1996) with the appropriate correction for the background estimation bug applied (Bertin 1998). SExtractor was chosen for its ability to detect objects in one image and analyze the corresponding pixels in a separate image; which, when applied uniformly to multi-band data, generates a matched aperture dataset. Our detection image was constructed from the $U, B, R, \& \ I$ images using a χ^2 process (Szalay *et al.* 1998). Briefly, this process involves convolving each input image with a Gaussian kernel matched to the seeing. The convolved images were squared, and normalized so that they had zero mean and unit variance. The four processed images (corresponding to the original $U, B, R, \& \ I$ images) were coadded, forming the χ^2 detection image. A histogram of the pixel distribution in the χ^2 image was created, and compared to a χ^2 function with four degrees of freedom (which corresponds to the sky pixel distribution). The "object" pixel distribution was generated by subtracting the "sky" pixel distribution from the actual pixel

distribution. The Bayesian detection threshold was set equivalent to the intersection of the "sky" and "object" distributions (*i.e.* where the object pixel flux becomes dominant). To convert this empirical threshold for use with SExtractor, we had to scale the threshold (which is a flux per pixel value) into a surface brightness threshold (which is in magnitudes per square arcsecond).

2.5. Completeness and Photometric Limits

Detecting and analyzing faint objects in an image is hindered by many different effects, including object superposition, noise fluctuations, as well as redshift and evolutionary effects. These factors can prevent objects from being detected (confidence), introduce false detections (contamination), and affect the accuracy of the photometric measurements. The standard method for quantifying the reduction in the detection efficiency is through a heavy utilization of simulations: either through the simulation of an entire image, or through the addition of simulated or real images to the actual object frame. In order to determine the completeness limits in a model independent manner, we adopted the latter approach.

We, therefore, added one hundred artificially generated galaxies to the final stacked image. The magnitudes of the artificial galaxies were drawn uniformly from a one half magnitude interval (*i.e.* $25.0 \leq U < 25.5$). The new image was processed in an identical manner to the original image, and the resultant catalog was cross-identified with the input artificial galaxy catalog using both a proximity and magnitude match criteria. This process was repeated ten times for each half-magnitude bin in each filter over the relevant range of magnitudes, and the mean and one sigma deviation were extracted using a high/low rejection for each half-magnitude bin. These data were used to determine the completeness correction curves (*cf.* Figure 2) by interpolating between the data points with a second order polynomial. From the interpolating function, both a 90% and 50% completeness

limits in all four bands were measured.

EDITOR: PLACE FIGURE 2 HERE.

Rather than relying on completeness limits, some analysis techniques require precise photometric measurements. In order to satisfy these conditions, we determined both the 2% and 10% photometric error magnitude limits. These limits for all four bands were calculated by scanning though the master catalog for all valid detections which had a measured photometric error that was approximately the same as the target photometric error (0.1 magnitudes for 10% photometry and 0.02 magnitudes for 2% photometry). The means of the magnitudes for all such selected galaxies were determined, and these values were designated as the magnitudes at which the photometric error reached the target error (*cf.* Table 1).

2.6. Astrometry

Traditionally, astrometry is performed by identifying calibrated stars within the image of interest. Often these stars are selected from the *HST* Guide Star Catalog (GSC) (Lasker *et al.* 1988). Within our stacked image, however, we could not reliably utilize the GSC calibrated stars, since there were not enough unsaturated GSC stars in our final stacked image. Fortunately, we were able to obtain an early release of the *HST* Guide Star Catalog II (Lasker 1996), which, although it is currently less precise than the original guide star catalog, had sufficient calibration candidates to properly determine an astrometric solution. The residuals of the final geometric transformation to the GSCII for the reference stars were all less than 0.15 pixels, or equivalently, less than $0.07''$.

2.7. Spectroscopic Cross-identification

To derive an empirical photometric redshift relation, a sample of calibrating redshifts are required. Two spectroscopic surveys: the Canada–France Redshift Survey (CFRS, Lilly *et al.* 1995), and the Deep Extragalactic Evolutionary Probe (DEEP, Mould 1993), have both obtained spectroscopic redshifts for objects within our catalog.

The CFRS spectroscopic targets were selected from a complementary CCD imaging survey to $I_{AB} \leq 22.5$. The spectroscopic observations were done using the Canada-France-Hawaii 3.5 meter telescope. The DEEP project is a multi-institution collaboration, in which we are participating, that is currently using the low resolution imaging spectrograph (LRIS) on the Keck II 10 meter telescope to obtain spectra for objects to $I \sim 24.0$. DEEP spectroscopic targets are predominantly selected from images obtained with the repaired *HST* wide field and planetary camera (WFPC2). The remaining spectroscopic targets are selected from existing ground based imaging.

The object match-up procedure with each spectroscopic catalog was done using a growing annulus technique where the angular distance ψ was determined using the formula $\psi = \arccos(\sin(\phi_s)\sin(\phi_p) + \cos(\phi_s)\cos(\phi_p)\cos(\theta_s - \theta_p))$, where the angles ($\theta \equiv$ Declination, $\phi \equiv$ Right Ascension) have been properly converted into radians, and the subscript s refers to spectroscopic target and the subscript p refers to photometric object. A magnitude restriction was also utilized to prevent improper identifications due to poor relative astrometry, blended objects, or false detections. As both spectroscopic surveys had I band magnitudes for the spectroscopic targets, the magnitude test was done using I magnitudes.

2.8. Star Galaxy Separation

In an effort to simplify the star–galaxy separation effort, we measured several different aperture magnitudes in addition to the "Kron" magnitude we use for the subsequent analysis. Of primary interest is the 2.5 pixel diameter aperture magnitude (matched to the median point spread function), which provides a measurement of the core flux of an object. The ratio of the core flux to the total object flux should be larger for the bright stellar objects than for non-stellar objects, as by definition, the majority of the flux of a point source is contained within the point spread function.

In order to determine an empirical algorithm for classifying stellar objects, we constructed a stellar object catalog from the spectroscopic catalogs, *HST* imaging, and these photometric data. Eighty two objects were selected from the stacked I band frame using the IRAF task `imexam` to measure the radial profiles of candidate objects. Only those objects with both a Gaussian profile and a high signal to noise peak flux were selected. Thirty additional objects were selected from the CFRS spectroscopic data which had a reliable redshift equal to zero, while an additional thirteen spectroscopic stellar objects were selected from the DEEP data. Finally, we used the *HST* images to identify twenty seven additional sources, providing a total of 152 stellar candidates to quantify the stellar locus.

In addition, all objects which had a total I magnitude brighter than twentieth magnitude were visually inspected and classified as stellar or non-stellar. We constructed bounding boxes around the classified stellar objects, providing empirical stellar classifications in each band (*cf.* Figure 3). The final classification was constructed by taking the union of the four separate classifications, resulting in 505 stellar objects. The number-magnitude distribution of stellar objects agrees with the predictions of the Bahcall-Soniera model (1980). The spatial distribution of the stellar objects is fairly random, with the possible minor exception of the image corners where the PSF increases due to focal degradations.

EDITOR: PLACE FIGURE 3 HERE.

3. Deep Multi-band Optical Number Counts

Counting the number of galaxies as a function of apparent magnitude is a simple, yet powerful statistic in understanding the evolution of galaxies. Measurements of the number-magnitude relation, however, have typically been hindered in two ways. First, the amount of sky surveyed was generally sacrificed in an effort to push the completeness limits imaged deeper. This can produce biases due to object clustering and sample variance. Second, most deep surveys do not fully sample the optical spectral region. This limits the amount of evolutionary information about the underlying galaxy population that can be reliably extracted.

We, therefore, present the measured number-magnitude counts in the optical bands $U, B, R, \& \ I$. This work is unique for the relatively large area ($\approx$ 196 Sq. Arcminute) that has been deeply imaged in multiple optical bands. As such, this dataset serves as a bridge between the large area, shallow photographic surveys, and the small area, deep fields such as the HDF (Williams *et al.* 1996).

3.1. Analysis

Detecting faint objects in an image is hindered by many different effects, including object superposition, noise spikes, as well as redshift and evolutionary effects. Furthermore, these complications strongly affect the number-magnitude relation. In order to reliably extend the measured galaxy counts fainter, corrections for the completeness of the survey and subsequent analysis must be applied. Invariably, this requires heavy utilization of

simulations: either through the simulation of an entire image, or through the addition of simulated images to the actual object frame. As we wanted to determine the differential number-magnitude relation in a model independent manner, we adopted the latter approach (*cf.* Section 2.5). Using the calculated completeness function, we applied the appropriate scale factor to each galaxy as it was added to the appropriate bin, rather than the entire bin uniformly. We estimated the errors in our sample by combining the effects of Poisson noise with the one σ completeness errors we derived from our simulations.

We set the absolute lower limit used in our analysis to $\sim 10^{3.5}$ objects/Magnitude/Sq. Degree, which corresponds to ≈ 100 galaxies detected within a given half-magnitude bin over the entire image, in order to limit the effects of poor statistics. We measured the slope for the full range using a simple least squares approach. As the corrected counts of the bluer bands indicated a change in the slope parameter (α), we also measured the slopes for the bright end (matching previous photographic surveys) and for the faint end (which we can compare to the HDF). Modeling the differential number magnitude counts as $dN(m) \propto m^{\alpha}$, we measure a change in the slope (α_B) in the B_{AB} band number magnitude relation at $B_{AB} \approx 24.4$ previously noted by other authors (Lilly *et al.* 1991, Metcalfe *et al.* 1995). We also measure a change in the U_{AB} band slope (α_U) at $U_{AB} \approx 24.7$, which has been suggested earlier (Majewski 1989). Interestingly, our bright slopes agree quite well with the photographic data (*cf.* Table 2), and although the two normalizations differ, the faint end slope of our ground based data also agrees with our measurements of the slope of the corresponding HDF band (Metcalfe *et al.* 1996). The most likely explanation for the difference in the faint end slopes lies in the differences in faint object detection and extraction between the different surveys (*cf.* the different number of objects detected in the HDF using different techniques Ferguson 1998.)

EDITOR: PLACE TABLE 2 HERE.

The measured number magnitude counts are presented in Figure 4 for the U band, Figure 5 for the B band, Figure 6 for the R band, and Figure 7 for the I band. In each of these figures, previously published number counts are also displayed.

EDITOR: PLACE FIGURE 4 HERE.

EDITOR: PLACE FIGURE 5 HERE.

EDITOR: PLACE FIGURE 6 HERE.

EDITOR: PLACE FIGURE 7 HERE.

4. Photometric Redshifts

To understand the evolution of the universe, a large, uniform spectroscopic sample must be utilized. The creation of such a sample is extremely difficult and currently impractical. Many cosmological tests, however, are more sensitive to the sample size (*i.e.* Poisson Noise) than small errors in distance — which makes them perfect candidates for utilizing a photometric redshift catalog. We have developed an empirical photometric redshift technique (Connolly *et al.* 1995, Brunner *et al.* 1997, Brunner 1997), which is not designed to accurately predict the redshift for a given galaxy (Baum 1962) or locate high redshift objects (Steidel *et al.* 1996). Instead, it is designed to provide distance indicators which are statistically accurate for the entire sample, along with corresponding redshift error estimates.

4.1. Calibration Data

The accuracy of any empirically derived relationship is predominantly dependent on the quality of the data used in the analysis — photometric redshifts being no exception. As a result, we imposed several restrictions on the calibrating data in order to minimize the intrinsic dispersion within the photometric redshift relationship. The calibration data was taken from the spectroscopic cross identification with both the CFRS 14 hour +52 field and the DEEP *HST* 5096 field (*cf.* Section 2.7).

The CFRS cross identification catalog consisted of 211 objects, while the DEEP calibrating data provided 188 galaxies, with 28 duplicates between the two. For all but two duplicate measurements, the mean of the two redshifts was used. One of the remaining two duplicates (which had quite discordant redshift measurements) was eliminated from the sample due to source confusion, while the DEEP redshift was used for the second (as it had a higher confidence) providing 370 spectral cross-identifications. The next restriction was to select all objects with $z > 0.0$ in order to remove the stellar objects, pruning the catalog to 275 galaxies.

Although the intrinsic error of a spectroscopic redshift is generally quoted as $\delta < 0.001$, in reality however, a redshift is accurate only when the spectral identification is also accurate. For the CFRS data, a redshift quality was generated from both the spectral type and the reliability of the redshift assigned (Le Fevre *et al.* 1995). The CFRS galaxies were then restricted to the following six quality classes: 3, 4, 8, 93, 94, 98, to guarantee that only objects with redshifts having a confidence greater than 95% were retained; similar, albeit less empirical, constraints were placed on the DEEP galaxies. The next step was to restrict the sample to those objects which were below the 10% photometric error limit (*cf.* Section 2.5 for more information). In the remaining data, four objects were found to have bad detection flags (*e.g.,* object near edge of frame, incomplete aperture data) and were

subsequently removed, while an additional four galaxies were above our high redshift cut-off of $z = 1.2$. The final spectroscopic calibration data consisted of 190 galaxies.

4.2. The Empirical Relationship

4.2.1. Background

The derivation of photometric redshifts from broadband photometry has been previously shown to be more sensitive to broad spectroscopic continuum features (primarily the break in the continuum spectra at around 4000 Å) rather than specific absorption/emission features (Connolly *et al.* 1995). As a result, we define five different redshift intervals (*cf.* Table 3) which track the movement of the 4000 Å break through our filter system with increasing redshift (*cf.* Figure 1). In the three intervals, low, medium, and high, we can accurately approximate the galaxy distribution in the four flux space $U, B, R, \& \ I$ by a second order polynomial. Between these selected redshift intervals, however, the continuum break is moving between adjacent filters, introducing a curvature in the galaxy distribution, necessitating the use of a third order polynomial to accurately map the galaxy distribution.

EDITOR: PLACE TABLE 3 HERE.

4.2.2. Algorithm

The 190 calibrating redshifts were, therefore, used to derive a global third order polynomial in $U, B, R, \& \ I$ which provided an initial redshift estimate. Likewise, second order polynomials in $U, B, R, \& \ I$ were determined for the three different redshift intervals, while third order polynomials were determined for the two break regions. The range of

calibrating redshifts for each polynomial fit was extended by approximately 0.05 in order to diminish end-aliasing effects. This algorithm is designed to generate an optimal redshift for objects by using the more accurate local relations (Brunner *et al.* 1997). For each derived polynomial fit, the degrees of freedom remained a substantial fraction of the original data (a second order fit in four variables requires 15 parameters while a third order fit in four variables requires 35 parameters).

4.3. Analysis of the Relationship

The relative importance of the different bands in the individual redshift intervals reflects the curvature inherent within the distribution of galaxies in the four dimensional flux space. In a given redshift range, the curvature can be accurately approximated by a second order polynomial. Between redshift intervals, however, the distribution displays a higher order curvature term (*cf.* the previous discussion concerning the continuum break), which requires the higher order fit. The correlation between the four band photometric and spectroscopic redshifts is shown in Figure 8. The intrinsic dispersion ($\delta z = 0.061$) is relatively stable throughout the redshift range spanned by the calibrating galaxies, and as shown in Figure 9, is clearly Gaussian in projection.

EDITOR: PLACE FIGURE 8 HERE.

EDITOR: PLACE FIGURE 9 HERE.

The overall accuracy with which we can estimate redshifts leads us to two related conclusions. First, this technique is extremely dependent at these redshifts on the 4000 Å break over the redshift interval sampled by the calibration data, which is present in

nearly all galaxies. Second, metallicity, dust, and age variations have similar effects in this multidimensional space, albeit almost orthogonal to the redshift vector (Koo 1986), and therefore affect the galaxy distribution, which we are attempting to model, in similar directions.

4.3.1. Aperture Effects

In a similar manner, we calculated photometric redshift relations for the four different fixed aperture magnitudes in our catalog (2.5 pixels, 5 pixels, 10 pixels and 20 pixels). We compare their intrinsic dispersions in Figure 10. Due to the strength of the 4000 Å continuum feature in determining the photometric redshift of an object, we decided to test the hypothesis that "bulge" magnitudes would produce a more accurate photometric redshift relationship. In no case did a fixed aperture magnitude reduce the dispersion over a total magnitude. The results, however, are encouraging, and worth a deeper examination.

EDITOR: PLACE FIGURE 10 HERE.

The two best relations are clearly the 5 and 10 pixel aperture magnitudes. In the I band, the median full width at half maximum for all objects with $I < 24.0$ is approximately 4.7 pixels. Thus, the 5 pixel aperture generally accounts for approximately 75% of the object, while the 10 pixel aperture accounts for approximately 98% of the typical object. As the aperture size is decreased, the effects of shot noise will become significant (since we are sampling only the core of an object). On the other hand, as the aperture size is increased, sky noise will begin to affect the relationship more strongly (since we are sampling the wings of the object flux distribution). Therefore, the total magnitudes that we use in our analysis are best approximated by the 10 pixel fixed aperture magnitudes, which sample the majority of an objects flux. Due to the effects of ground based seeing, however, we

can not reliably estimate a bulge magnitude due to the faint nature of the galaxies in our sample. This approach, however, might prove more useful for space-based data (*i.e. HST*).

4.3.2. Selection Effects

A subtle, and often overlooked, effect in any photometric redshift analysis is the requirement for accurate multi-band photometry. Ideally we could restrict our photometric-redshift catalog to only those objects which have measured magnitude errors below some set limits (*e.g.,* 10% photometry). This type of a restriction, however, introduces two complications: a bias towards blue spectral types, and a subsequently complicated selection effect (*cf.* Figure 11).

EDITOR: PLACE FIGURE 11 HERE.

In an attempt to overcome these biases, we restrict the full sample to those objects which have both $I_{AB} < 24.0$ and measured magnitude errors < 0.25 in $U, B, \& R$. This minimizes any selection bias to only faint early-type galaxies. In Figure 12, the effects of this cut can be discerned, and from the bottom panel (which models our final selection criteria), it is fairly evident that this particular selection results in a sample that is I band limited with a high redshift cut from the Lyman break systems (*i.e.* U and B band drop-outs). The remaining filter combinations contribute to the noise in our analysis (*i.e.* when we consider our final catalog complete to $I \approx 24.0$), and amount to only a few percent when combined. The final catalog contains 3612 sources, of which 442 are classified as stellar objects, and a remaining 118 sources had bad detection flags (*e.g.,* edge of frame, incomplete aperture data). Our final photometric-redshift catalog, therefore, contains 3052 sources.

EDITOR: PLACE FIGURE 12 HERE.

4.4. Error Analysis

4.4.1. Intrinsic Error Analysis

By directly comparing the estimated photometric–redshift with the measured spectroscopic redshift, we can estimate the precision with which we have quantified the topology of the galaxy distribution in the four band flux space $U, B, R, \& \ I$. When estimating redshifts for objects with no spectroscopic redshifts (which is the goal of this analysis) what is desired is an independent estimate of the error in the photometric redshift.

In order to determine the optimal error estimate for galaxies with no spectroscopic redshift, we developed a bootstrap error estimation techniques that would generate multiple realizations of the photometric redshift relation from which we could test various error estimators. The fundamental principles behind this technique are to model the effects of removing calibrating galaxies from the sample, while simultaneously including the effects of the photometric errors. This will simulate the possible effects of an incomplete sampling of the distribution in flux space by the calibrating galaxies.

Algorithmically, the calibration sample is randomly divided into two samples, new calibration data, and test data. Although random, the division is devised so that the calibrating sample is divided into 15 bins, with 14 of the bins ($\approx$ 177 galaxies) used to calibrate the relationship, and the remaining bin ($\approx$ 13 galaxies) used to test the new relationship. This algorithm was implemented in Mathematica (Wolfram 1996), and 1000 iterations were produced. If the division process was truly random, each galaxy would have a probability of being selected of 1/15 for each iteration, and, therefore, in 1000 iterations, each galaxy should be selected on average 67 times. The actual statistics compare quite

well, as the mean of the selection distribution was ≈ 65, the standard deviation was ≈ 20, while the minimum number of times a galaxy was selected was 43 and the maximum number was 185.

Every time a galaxy was a member of the test sample, its estimated redshift was appended to the list of estimated redshifts for that galaxy. After the completion of the 1000 iterations, the following quantities were calculated for every calibration object from the list of estimated redshifts: the mean of the estimated redshifts, the trimmed (one sigma deviations from the actual mean) mean, the standard deviation of the estimated redshifts, and the six quantiles (uniformly spaced in σ) at the values: 0.0228 (Q_1), 0.1587 (Q_2), 0.3085 (Q_3), 0.6915 (Q_4), 0.8413 (Q_5), 0.9772 (Q_6).

The six quantiles and the standard deviation of the distribution can be used to define four independent error estimators. The advantage of using the quantiles to estimate the standard deviation of a distribution is that they are much less sensitive to extreme outliers. Since the derivation of the photometric redshift relationship is more dependent on certain calibrating redshifts (due to the the incomplete sampling of the topology of the galaxy distribution in the four dimensional flux space $U, B, R, \& \ I$ by the calibrating galaxies), the quantile error estimators are, on average, more precise estimates of the redshift error than the standard deviation of the distribution. After a lengthy comparison, we defined the error of a photometric redshift to be $\sigma_z = (Q5 - Q2)/2.0$. This was due in part to its tighter correlation with δz than both the standard deviation and the Q_{6-1} error estimator, and also because the Q_{5-2} error estimator samples a larger number of data points than the Q_{4-3} error estimator due to its larger width (*cf.* Figure 13).

EDITOR: PLACE FIGURE 13 HERE.

A comparison between the defined error estimator and the four different magnitudes

(*cf.* Figure 14) demonstrates the sensitivity of the empirical fitting procedure on the calibration sample. At both limits, the distribution of galaxies is not fully sampled, and as a result, the estimated error is consequently larger. The estimated error distribution is also affected by the increase in photometric error at fainter magnitudes.

EDITOR: PLACE FIGURE 14 HERE.

4.4.2. Extrinsic Error Analysis

To estimate the error in a photometric redshift for the full photometric sample, we adopt a similar error estimation technique. Different realizations of the photometric redshift relationship are determined by adopting a bootstrap with replacement algorithm, in which galaxies are randomly selected from the calibration sample and, once selected, are not removed from the set of calibrating galaxies. Thus, at the extremes, one galaxy could be selected 190 consecutive times or, alternatively, each redshift could be selected exactly once (each of these realizations has the same probability). This approach is designed to emphasize any incompleteness in the sampling of the true distribution of galaxies in the four dimensional space $U, B, R, \& \ I$ by the calibration redshifts. As before, with each different realization, the magnitudes of the calibrating sample were drawn from a Gaussian probability distribution function with mean given by the measured magnitude and sigma by the magnitude error.

This algorithm was implemented in Mathematica, and 100 different realizations of the photometric redshift relationship were derived. For each different realization, a photometric redshift was calculated for every galaxy in the photometric redshift catalog. The six quantiles at the values: 0.0228 (Q_1), 0.1587 (Q_2), 0.3085 (Q_3), 0.6915 (Q_4), 0.8413 (Q_5), 0.9772 (Q_6), were computed from the 100 different redshift estimates for each

object. The error in the photometric redshift for each object was defined, as before, by $\sigma_z = (Q5 - Q2)/2.0$.

The photometric redshift and corresponding error are compared in Figure 15. As expected the average estimated error is the largest at the upper and lower redshift limits where the incompleteness in the calibrating sample is most evident. The majority of the rest of the objects with extremely large redshift errors are blended in one or more bands (there are 361 objects with $\sigma_Z > 0.5$ and 86% of them are blended or contaminated by nearby objects). As a result, objects which are affected by neighboring objects are isolated from the high density surface delineated by the majority of galaxies in the four flux space $U, B, R, \& \ I$. The affect these objects impart on any subsequent analysis, however, is minimized by the inclusion of their photometric error, which causes them to be non-localized in redshift space. As a result, these objects provide a minimal contribution to many "redshift bins" rather than strongly biasing only a few bins.

EDITOR: PLACE FIGURE 15 HERE.

On the other hand, those objects which are not blended, and still have large estimated redshift errors could define an extremely interesting sample for spectroscopic study (*i.e.* QSO's or active galaxies). This follows from the fact that by their very nature, these types of objects are unlike the majority of galaxies in the universe.

5. Spectral Classification

In addition to having an estimate for the redshift for each galaxy, evolutionary trends can be discussed in terms of the different types of observed galaxies present within the universe. For low redshifts, galaxies are often segregated based upon their morphology (*i.e.*

the Hubble sequence). At moderate to higher redshifts, however, morphological typing is extremely difficult, especially for ground based imaging. As a result, we adopt a different approach, which classifies galaxies by the spectral type which best matches their observed magnitudes.

5.1. Synthetic Magnitudes

The calculation of synthetic magnitudes from spectral energy distributions (SEDs) is based on the definition of apparent magnitudes.

$$m = -2.5 \log \left(\int f_\lambda R_\beta(\lambda) d\lambda \right) - m_0 \tag{1}$$

where f_λ is the absolute spectral energy distribution of the object in units of erg cm^{-2} s^{-1} Å^{-1}. $R_\beta(\lambda)$ is the system response function for filter $\beta \in \{ U\ ,\ B\ ,\ R\ ,\ I \}$ which we take as the convolution of the CCD quantum efficiency and the appropriate filter response function. m_0 is the zeropoint for the system, which is generally derived for $\alpha Lyrae$ (Vega). We transformed our calculated synthetic magnitudes to the AB system (Oke & Gunn, 1983) which introduces a zeropoint shift Δ_{AB} given by computing the synthetic AB magnitudes for $\alpha Lyrae$ in each filter (Frei and Gunn 1994): $\Delta_{AB}(U\ ) = 0.730$, $\Delta_{AB}(B\ ) = -0.055$, $\Delta_{AB}(R\ ) = 0.187$, and $\Delta_{AB}(I\ ) = 0.439$.

We, therefore, calculated magnitudes in a filter β given a spectral energy distribution,

$$m^\beta_{AB} = -2.5 \log \left(\int f_\lambda R_\beta(\lambda) d\lambda \right) - m^\beta_0 + \Delta_{AB}$$

where the zeropoints are $m^U_0 = 15.20$, $m^B_0 = 13.89$, $m^R_0 = 14.17$, and $m^I_0 = 15.16$.

5.2. Template Spectral Energy Distributions

In order to match the full range of observed magnitudes in the photometric redshift catalog, we required template spectra which extend to $\lambda = 3100$ Å$/2.2 \approx 1400$ Å, where 3100 Å is the approximate blue cut-off for the U filter. Rather than generating model template spectra to classify galaxies, we selected the Coleman, Wu, and Weedman (1980) UV-optical template spectra constructed from real galaxy spectra. The sample includes Irregular, Scd, Sbc, and Elliptical spectral energy distributions. The four template spectra are compared in Figure 16 in which the spectra smoothed over 10Å, and normalized to the Elliptical flux at $\lambda = 5500$Å.

EDITOR: PLACE FIGURE 16 HERE.

Synthetic AB magnitudes for the four template spectra were calculated for redshifts from $z = 0.0$ to $z = 1.2$ in steps of $\Delta z = 0.05$. This involves both redshifting each template spectra so that $\lambda' = \lambda/(1+z)$, and reducing the flux by a factor of $(1+z)$.

5.3. Spectral Classification Algorithm

To determine a spectral classification for each object, we need to optimally select a spectral energy distribution from the grid of redshifted template spectra. Algorithmically, we need to select the best fit to our data for different models, which is most easily done using chi-square fitting (Press *et al.* 1992). The optimal spectral energy distribution will, therefore, minimize the chi-squared statistic:

$$\chi^2 = \sum_{\beta}^{4} \left(f_\nu^\beta - \gamma t_\nu^\beta \right)^2$$

where $\beta \in \{ U\ ,\ B\ ,\ R\ ,\ I\ \}$, f_ν^β is the flux for the target object in the β filter, and t_ν^β is the flux for the current template spectra in the β filter. The constant γ is determined by

minimizing the variation of χ^2 with respect to γ, which gives:

$$\gamma = \frac{\sum_\beta (f_\nu^\beta t_\nu^\beta)}{\sum_\beta (t_\nu^\beta)^2}$$

This classification technique is essentially an inverted template SED photometric redshift calculation. The quantities γ, and χ^2 are computed for each of the redshift-selected template spectra from the object's observed broadband AB magnitudes and magnitude errors (*i.e.* to include the effects of photometric errors). This process was extended to include the estimated redshift errors, by selecting the redshift of a particular object from a Gaussian probability distribution function with mean and sigma given by the object's estimated redshift and redshift error. This was performed one hundred times for each object, resulting in one hundred different spectral classifications. The particular template which had the smallest χ^2 was then selected as the optimal SED for that object.

The different percentages of each spectral type are compared in Figure 17. Clearly the bluer spectra dominate the classification. This should not be interpreted as evidence for an overwhelming dominance of ultra luminous galaxies in this sample, particularly in light of our bias against early type galaxies. Instead, the best interpretation is that from the four template spectra originally selected for this analysis, the redshifted SEDs of nearby starbursting galaxies best match the observed data. In fact, this result demonstrates that galaxies tend to become bluer with redshift (*i.e.* the faint blue galaxy problem). Other examples of this are seen in the CFRS luminosity functions (Lilly *et al.* 1995) and the HDF morphological number counts (Driver *et al.* 1998).

EDITOR: PLACE FIGURE 17 HERE.

To form an impression of the accuracy of this spectral classification, each template was compared to the objects which were assigned to that template in two different

colors: $U_{AB} - I_{AB}$ (Figure 18), which presents the largest spectral baseline; and $(B_{AB} + R_{AB})/2.0 - I_{AB}$ (Figure 19), which is an interpolated V_{AB} band magnitude. For all four templates, the data clearly agree quite well, indicating that the classification algorithm is working properly.

EDITOR: PLACE FIGURE 18 HERE.

EDITOR: PLACE FIGURE 19 HERE.

6. Application: $N(z_P)$

We can derive the number of galaxies as a function of redshift, $N(z_P)$, as an example of a statistical application of photometric redshifts. First, we computed the number redshift distribution (in the traditional fashion) for redshift bins of width 0.1 magnitude. The resulting histogram is compared with the measured number-redshift distribution for the combined DEEP and CFRS samples in Figure 20. Since photometric redshifts are not equivalent to spectroscopic redshifts, this is clearly not the optimal method.

EDITOR: PLACE FIGURE 20 HERE.

An analytic method for estimating the number redshift distribution using photometric redshifts can be used to provide a more realistic redshift distribution. We define the probability density function, $P(z)$, for an individual galaxy's redshift to be a Gaussian probability distribution function with mean (μ) given by the estimated photometric redshift and standard deviation (σ) defined by the estimated error in the photometric redshift.

$$P(z) = \frac{1}{\sigma\sqrt{2\pi}} e^{\left(-\frac{(z-\mu)^2}{2\sigma^2}\right)}$$

When constructing the number redshift distribution, the cumulative distribution function for each galaxy is calculated over each redshift bin. This requires numerically integrating the probability density function, which is given by the Error function, $erf(z_P)$, for each galaxy between the endpoints of each redshift bin.

A formal, analytic technique, however, is not always available to utilize photometric redshifts and their associated errors when measuring cosmologically interesting quantities. As a result, we have developed an alternative technique, the galaxy ensemble approach. Essentially, we treat the problem in the context of statistical mechanics, where each galaxy is localized in redshift space by a Gaussian probability distribution function. To calculate a physically meaningful quantity, we create multiple realizations (or ensembles) of the galaxy redshift distribution, and calculate the appropriate quantity for all of the different ensembles. We then average the different measurements to produce the desired value, simultaneously producing a realistic error estimate.

To demonstrate the viability of this technique, we calculated the number redshift distribution as a function of spectral type, both analytically and using the ensemble approach. From Figure 21, the two distributions show remarkable agreement, both with each other as well as the spectroscopic number redshift distribution, with the benefit of the ensemble error estimate demonstrated (*i.e.* error bars). The differences in the redshift distributions of the different spectral types, which were computed as outlined in Section 6, such as the selection bias against Elliptical galaxies, are also visible.

EDITOR: PLACE FIGURE 21 HERE.

7. Conclusion

In this paper we have presented the statistical technique to quantify galaxy evolution. We also presented the photometric data which we have used to develop this technique. Using the number magnitude test, we have verified the validity of our catalog, and demonstrated the turnover in the U and B band number counts previously discussed. The empirical photometric redshift relation we derived has an intrinsic dispersion of $\delta z = 0.061$ out to $z = 1.2$, and is Gaussian in projection.

In order to more realistically quantify the evolution of galaxies, we also developed techniques to estimate the error in a photometric redshift, and classify the catalog objects by spectral type. To demonstrate the effectiveness of this approach, we presented the number redshift distribution as a function of spectral type using two different techniques: the analytic approach, and the ensemble approach. In the future, we plan on using the ensemble approach to measure the evolution of the luminosity function and the angular correlation function with redshift and spectral type (Brunner 1997, Connolly *et al.* 1998).

First we wish to acknowledge Gyula Szokoly for assistance in obtaining the data. We also would like to thank Barry Lasker, Gretchen Greene, and Brian McLean for allowing us access to an early version of the GSC II. We also wish to acknowledge useful discussions with Mark Dickinson, George Djorgovski, Mark Subbarao, and David Koo. We would also like to thank the referee, Rich Kron, for valuable suggestions on improving this work. RJB would like to acknowledge support from the National Aeronautics and Space Administration Graduate Student Researchers Program. AJC acknowledges partial support from NASA grant AR-06394.01-95A. ASZ has been supported by the NASA LTSA program.

REFERENCES

Bahcall, J.N., & Soneira, R.M., 1980, ApJS, 44, 73.

Baum, W.A. 1962, Problems of Extragalactic Research, IAU Symposium No. 15., 390.

Bertin, E., & Arnout, S., 1996, A&AS, 117, 393.

Bertin, E., 1998, Private Communication.

Brunner, R.J, PhD. Thesis, The Johns Hopkins University, 1997.

Brunner, R.J, Connolly, A.J., Szalay, A.S., & Bershady, M.A., 1997, ApJ, 482, L21.

Bruzual, G.A., & Charlot, S., 1993, ApJ, 405, 538.

Coleman, G.D., Wu, C.C., & Weedman, D.W., 1980, ApJS, 43, 393.

Connolly, A.J., Csabai, I., Szalay, A.S., Koo, D.C., Kron, R.G., and Munn, J.A., 1995, AJ, 110, 6.

Connolly, A.J., Szalay, A.S., and Brunner, R.J., 1998, ApJ, 499, L125.

Couch, W.J., & Newell, E.B., 1984, ApJS, 56, 143.

Driver, S.P., Phillipps, S., Davies, J.I., Morgan, I., Disney, M.J., 1994, MNRAS, 266, 155.

Driver, S.P., Fernandez-Soto, A., Couch, W.J., Odewhan, S.C., Windhorst, R.A., Phillips, S., Lanzetta, K., and Yahil, A., 1998, ApJ, 496, 93.

Ferguson, H.C., 1998, in M. Livio, S.M. Fall, and P. Madua editors, *The Hubble Deep Field*,p. 181, Number 11 in the STSCI Symposium Series, Cambridge Academic Press.

Frei, Z., and Gunn, J.E., 1994, AJ, 108, 1476.

Fukugita, M., Shimasaku, K., Ichikawa, T., 1995, PASP, 107, 945.

Guhathakurta, P., Tyson, J.A., & Majewski, S.R.,1990, ApJ, 357, 9.

Gwyn, S.D.J., & Hartwick, F.D.A, 1996, ApJ, 440, 470.

Hall, P., & Mackey, C.D., 1984, MNRAS, 210, 979.

Infante, L., Pritchet, C., Quintana, H., 1986, AJ, 91, 217.

Jarvis, J.F., & Tyson, J.A., 1981, AJ, 86, 476.

Jones, L.R., Fong, R., Shanks, T., Ellis, R.S., Peterson, B.A., 1991, MNRAS, 249, 481.

Kinney, A.L., Calzetti, D., Bohlin, R.C., McQuade, K., Storchi-Bergmann, T., & Schmitt, H.R., 1996, ApJ, 467, 38.

Koo, D.C., 1985, AJ, 90, 418.

Koo, D.C., 1986, ApJ, 311, 651.

Kron, R.G., 1980, ApJS, 43, 305.

Landolt, A.U. 1992, AJ, 104, 340.

Lanzetta, K.M., Yahil, A., & Fernandez-Soto, A., 1996, Nature, 381, 759.

Lasker, B.M., Sturch, C.R., Lopez, C., Mallamas, A.D., Mclaughlin, S.F., Russell, J.L., Wisniewski, W,Z, Gillespie, B.A., Jenkner, H., Siciliano, E.D., Kenny, D., Baumert, J.H., Goldberg, A.M., Henry, G.W., Kemper, E., Siegel, M.J., 1988, ApJS, 68, 1.

Lasker, B., 1996, Private Communication.

Le Fevre, O., Crampton, D., Lilly, S.J., Hammer, F., & Tresse, L., 1995, ApJ, 455, 60.

Lilly, S.J., Cowie, L.L., Gardner, J.P., 1991, ApJ, 390, 79.

Lilly, S.J., Hammer, F., Crampton, D., & Le Fevre, O., 1995, ApJ, 455, 75.

Loh, E.D., & Spillar, E.J., 1986, ApJ, 303, 154.

Majewski, S.R., 1989, In C.S. Frenk, R.S. Ellis, T. Shanks, A.F. Heavens, and J.A. Peacock, editors, *The Epoch of Galaxy Formation*, pages 85–88. Kluwer.

Massey, P., Armandroff, T., De Veny, J., Claver, C., Harmer, C., Jacoby, G., Schoening, B., & Silva, D., 1996, *Direct Imaging Manual for Kitt Peak*.

Metcalfe, N., Shanks, T., Fong, R., & Roche, N., 1995, MNRAS, 273, 257.

Metcalfe, N., Shanks, T., Campos, A., Fong, R., & Gardner, J.P., 1996, Nature, 383, 236.

Mobasher, B., Rowen-Robinson, M., Georgakakis, A., & Eaton, N., 1996, MNRAS, 282, L7.

Mould, J.R., 1993, In B.T. Soifer, editor, *Sky Surveys: Protostars to Protogalaxies*, number 43 in ASP Conference Series.

Oke, J.B., & Gunn, J.E., 1983, ApJ, 266, 713.

Press, W.H., Teukolsky, S.A., Vetterling, W.T., & Flannery, B.P., 1992, *Numerical Recipes in C*, Cambridge University Press, 2 edition.

Sawicki, M.J., Lin, H., & Yee, H.K.C., 1997, AJ, 113, 1.

Shanks, T., Stevenson, P.R.F., Fong, R., Macgillivray, H.T., 1984, MNRAS, 206, 767.

Smail, I., Hogg, D.W., Yan, L., and Cohen, J.G. 1995, ApJ, 449, L105.

Steidel, C.C., & Hamilton, D., 1993, AJ, 105, 2017.

Steidel, C.C., Giavalisco, M., Pettini, M., Dickinson, M., & Adelberger, K.L., 1996, ApJ, 462, L17.

Szalay, A.S., Connolly, A.J., & Szokoly, G.P., 1998, submitted.

Tyson, J.A., 1988, AJ, 96, 1.

Williams, R.E., Blacker, B., Dickinson, M.E., Dixon, W., Ferguson, H.C., Fruchter, A.S., Giavalisco, M., Gilliland, R.L., Heyer, I., Katsanis, R., Levay, Z., Lucas, R.A., McElroy, D.B., Petro, L., Postman, M., Adorf, H., & Hook, R., 1996, AJ, 112, 1335.

Wolfram, S., 1996, *The Mathematica Book*, Cambridge University Press.

This manuscript was prepared with the AAS LaTeX macros v4.0.

Fig. 1.— The effective transmission for the standard broadband filters $U, B, R, \& I$ available for use at the KPNO 4 meter. The dashed lines are the individual filter transmission curves, the dotted line is the CCD detection quantum efficiency curve, and the solid curves are the convolution of the filter and detector quantum efficiency. Across the top is displayed the equivalent redshift of the 4000 Å break. The data points were obtained via anonymous FTP from the KPNO archives.

Fig. 2.— The fractional completeness curves for all four bands. The short dashed line in each figure is the 90% completeness limit, and the long dashed line is the 50% completeness limit. The starred points are the values derived from the simulations. The curves are the second order interpolating polynomial fits to the points determined from simulations.

Fig. 3.— The I Band stellar classification. The small dots are all of the galaxies in the catalog. The dotted line delineates the stellar classification criteria. The large circles indicate objects which are from the classification training set. The remaining symbols: diamond, plus, left triangle, and right triangle, indicate objects that were classified as stars in the I , R , B , & U bands, respectively.

Fig. 4.— The U Band number counts. Also plotted are comparable published counts, and the global fit (dashed line) and high/low fits (solid lines). The inset in the lower left corner indicates the errors and fits in more detail.

Fig. 5.— The B Band number counts. Also plotted are comparable published counts, and the global fit (dashed line) and high/low fits (solid lines). The inset in the lower left corner indicates the errors and fits in more detail.

Fig. 6.— The R Band number counts. Also plotted are comparable published counts, and the global fit (dashed line). The inset in the lower left corner indicates the errors and fits in more detail.

Fig. 7.— The I Band number counts. Also plotted are comparable published counts, and the global fit (dashed line). The inset in the lower left corner indicates the errors and fits in more detail.

Fig. 8.— Correlation between photometric and spectroscopic redshifts for the entire calibration sample. The straight line is of unit slope, and is not a fit to the actual data.

Fig. 9.— A histogram of the residual differences between photometric and spectroscopic redshifts for the entire calibration sample.

Fig. 10.— A comparison between the aperture magnitude photometric redshifts and the calibrating spectroscopic redshift sample.

Fig. 11.— The selection effect that results from requiring accurate four band photometry. In each figure, the dash-dot line is the U band 10% photometric limit, while the long dash line is the I band 10% photometric limit. The two curves trace the $U - I$ color for a source of a given SED type that has a U band magnitude at the 10% photometric limit (dotted line) and 25% photometric limit (solid line). The exclusion of the early types at moderate to large redshifts is clearly present. The other types, however, are clearly not excluded at any redshift in our final catalog.

Fig. 12.— The band distribution of sources with $I_{AB} < 24.0$ and 10% photometric errors (top panel) and 25% photometric errors (bottom panel). The horizontal axis indicates the photometric errors in the other three bands (U B R). The first bin contains the objects which have magnitude errors greater than the appropriate limit (or were not even detected in a band). Note the two secondary peaks in the bottom panel at R and BR. A closer inspection reveals that a majority of these sources are most likely U and B drop-out systems (Steidel *et al.* 1996). The small size of the other bins demonstrates their contribution to the statistical noise in our analysis.

Fig. 13.— A comparison between the different error estimates and the spectroscopic redshift. The figure has been trimmed for clarity to display only those sources with errors less than 0.45. This eliminated 14 objects from the top left figure, 12 objects from the top right figure, 10 from the bottom left figure and 6 from the bottom right figure. The estimated error can be quite large where the number of calibrating galaxies is insufficient to model the galaxy distribution in flux space.The Q_{5-2} error estimate (bottom left) has the smallest scatter.

Fig. 14.— A comparison between the photometric redshift error estimator and the magnitudes of the calibrating galaxies. The figures have been trimmed for clarity, removing 10 calibrators.

Fig. 15.— Correlation between photometric redshifts and the estimated redshift error for the significant catalog objects. Of the total sample of 3052 sources, 113 have photometric redshifts outside the range $z \in [0.0, 1.2]$. Also plotted are the median (solid line) and mean (dotted line) of the estimated photometric redshift errors, binned by 0.2 in redshift. The increase in both the mean and median of the binned estimated redshift error, reflect the built-in error correction, as these objects are down-weighted in any analysis since their redshift probability distribution functions are non-localized.

Fig. 16.— The template spectra normalized to the Elliptical template flux at 5500 Å and smoothed over 100 Å.

Fig. 17.— The SED Percentage of total sample. Note that the Elliptical types are diminished relative to the field due to the four band selection effect.

Fig. 18.— A comparison between the templates and the classified sources in the U - I color.

Fig. 19.— A comparison between the templates and the classified sources in an interpolated V - I color.

Fig. 20.— A comparison between the actual number-redshift relation (top) defined by the combined DEEP and CFRS calibrating redshift sample (solid line) and the full spectroscopic sample (dashed line), and the number-redshift relation for the full photometric sample using redshift intervals of 0.1 magnitudes.

Fig. 21.— The number-redshift distribution for both the full sample as derived from 100 different ensembles including the one sigma errors and the full sample derived analytically, as well as a function of spectral type. Each distribution has been normalized by the total number of galaxies in the distribution and scaled to percentages.

Table 1. The integration times for each of the four filters and the corresponding completeness and photometric magnitude limits.

Filter	Integration Time (s)	90%	50%	$\sigma \approx 0.02$	$\sigma \approx 0.1$
U	40129	25.94	26.65	23.74	25.92
B	16680	25.26	26.49	23.25	25.64
R	4500	24.45	25.41	22.70	24.66
I	4200	23.97	24.74	22.03	23.94

Table 2. The completeness limits, turnover point, and measured slopes for the number-magnitude relationships from our CCD data, published photographic surveys, and the HDF.

Band	50%	90%	Turnover	α_{Full}	α_{Low}	α_{High}	α_{Photo}[a]	α_{HDF}[b]
U_{AB}	25.94	26.65	24.68	0.40	0.51	0.24	0.6	0.23
B_{AB}	25.26	26.49	24.45	0.39	0.51	0.22	0.5	0.24
R_{AB}	24.45	25.41	—	0.34	—	—	0.4	0.24
I_{AB}	23.97	24.74	—	0.32	—	—	0.4	0.25

[a]Slopes published by David Koo (1986)

[b]These slopes are our own fits to published corrected counts provided by N. Metcalfe (1996). The magnitude range used was set to minimize the low statistics at the bright end, and the incompleteness at the faint end.

Table 3. The algorithmic details for generating the final photometric redshift from the initial estimate generated from the global third order fit. The fit region is the range of global redshift estimates over which the local fit is applied. The calibration region indicates the range of calibration redshifts used to constrain the local fit.

Interval Name	Fit Region	Calibration Region
Low	$z \leq 0.25$	$(0.0, 0.4]$
Low Break	$0.25 < z \leq 0.5$	$(0.2, 0.55]$
Medium	$0.5 < z \leq 0.7$	$(0.4, 0.8]$
High Break	$0.7 < z \leq 0.9$	$(0.6, 1.0]$
High	$0.9 < z$	$(0.8, 1.2]$

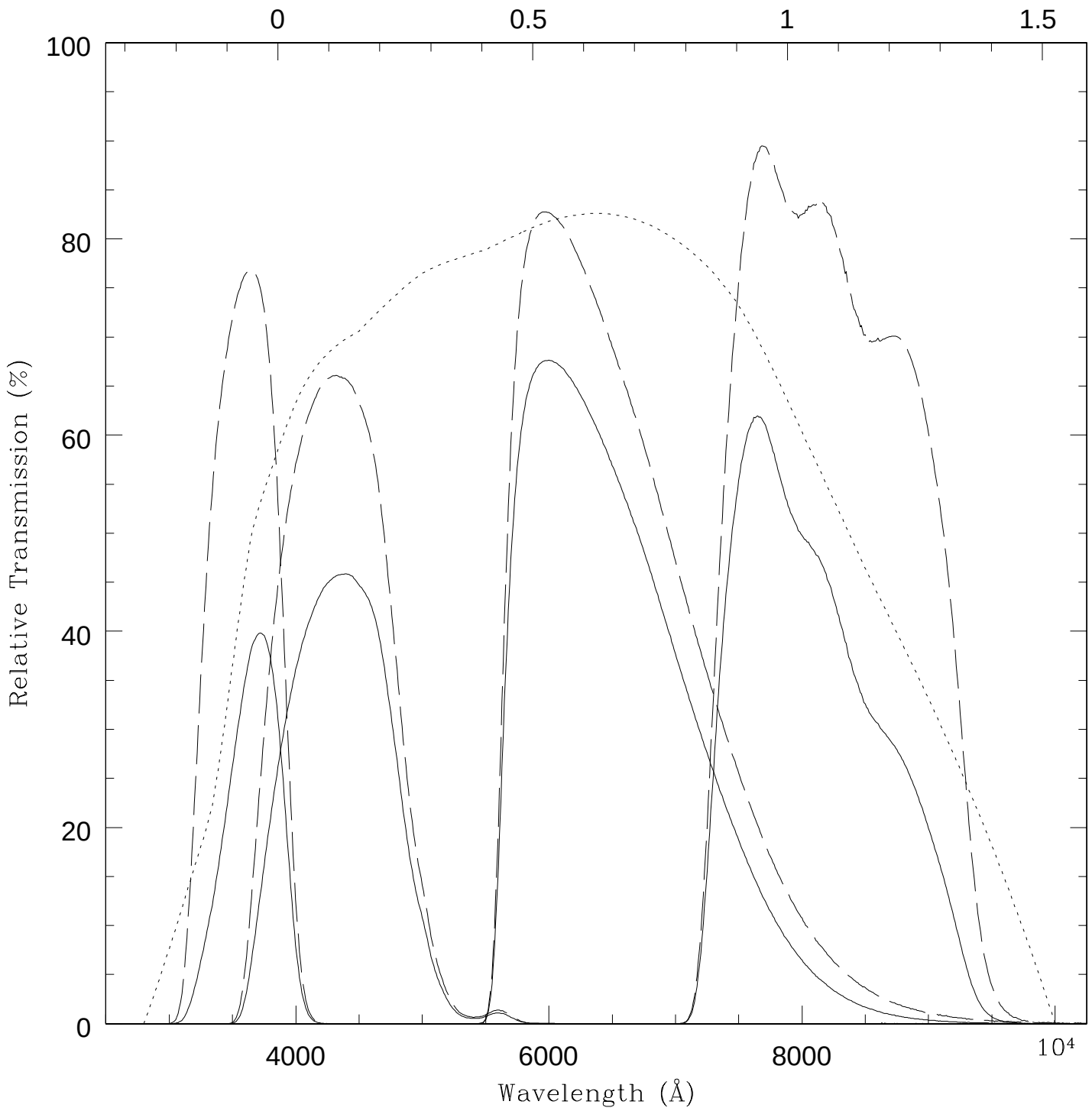
0
0.5
1
1.5
100
80
60
40
20
0
Relative Transmission (%)
4000
6000
8000
10⁴
Wavelength (Å)

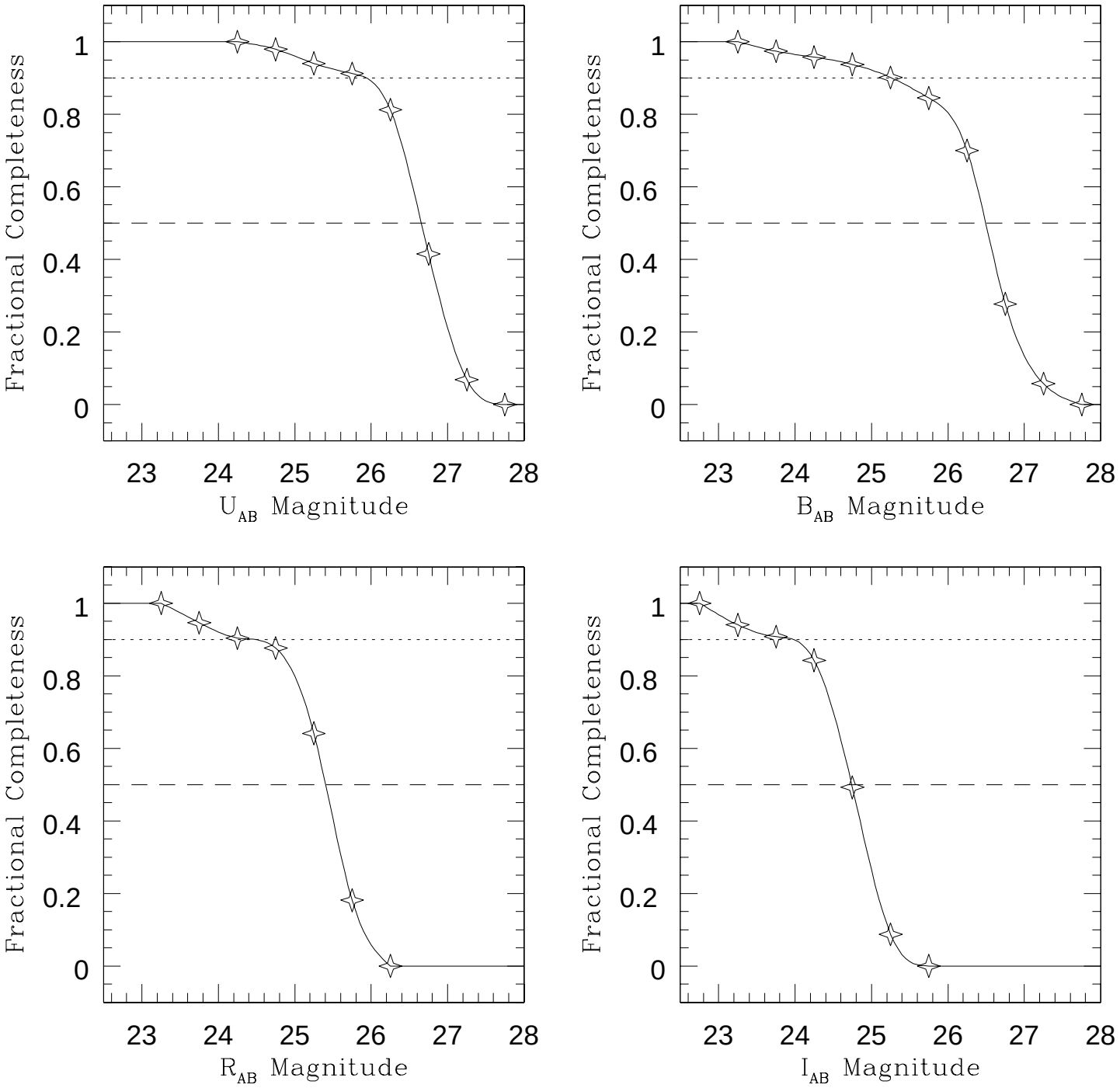
Fractional Completeness
0
0.2
0.4
0.6
0.8
1
23
24
25
26
27
28
U_{AB} Magnitude
B_{AB} Magnitude
R_{AB} Magnitude
I_{AB} Magnitude

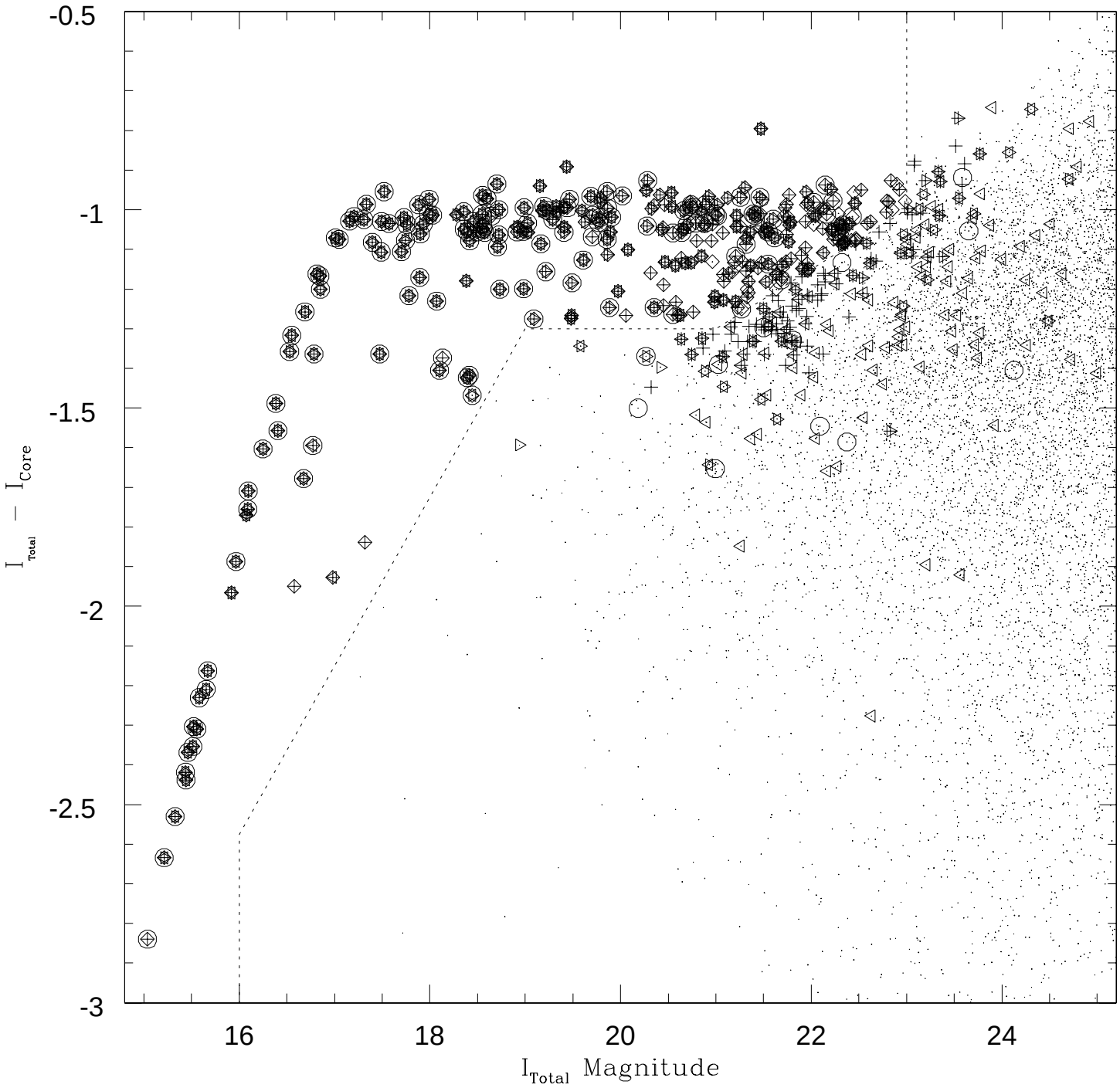
-0.5
-1
-1.5
-2
-2.5
-3
16
18
20
22
24
$I_{Total} - I_{Core}$
I_{Total} Magnitude

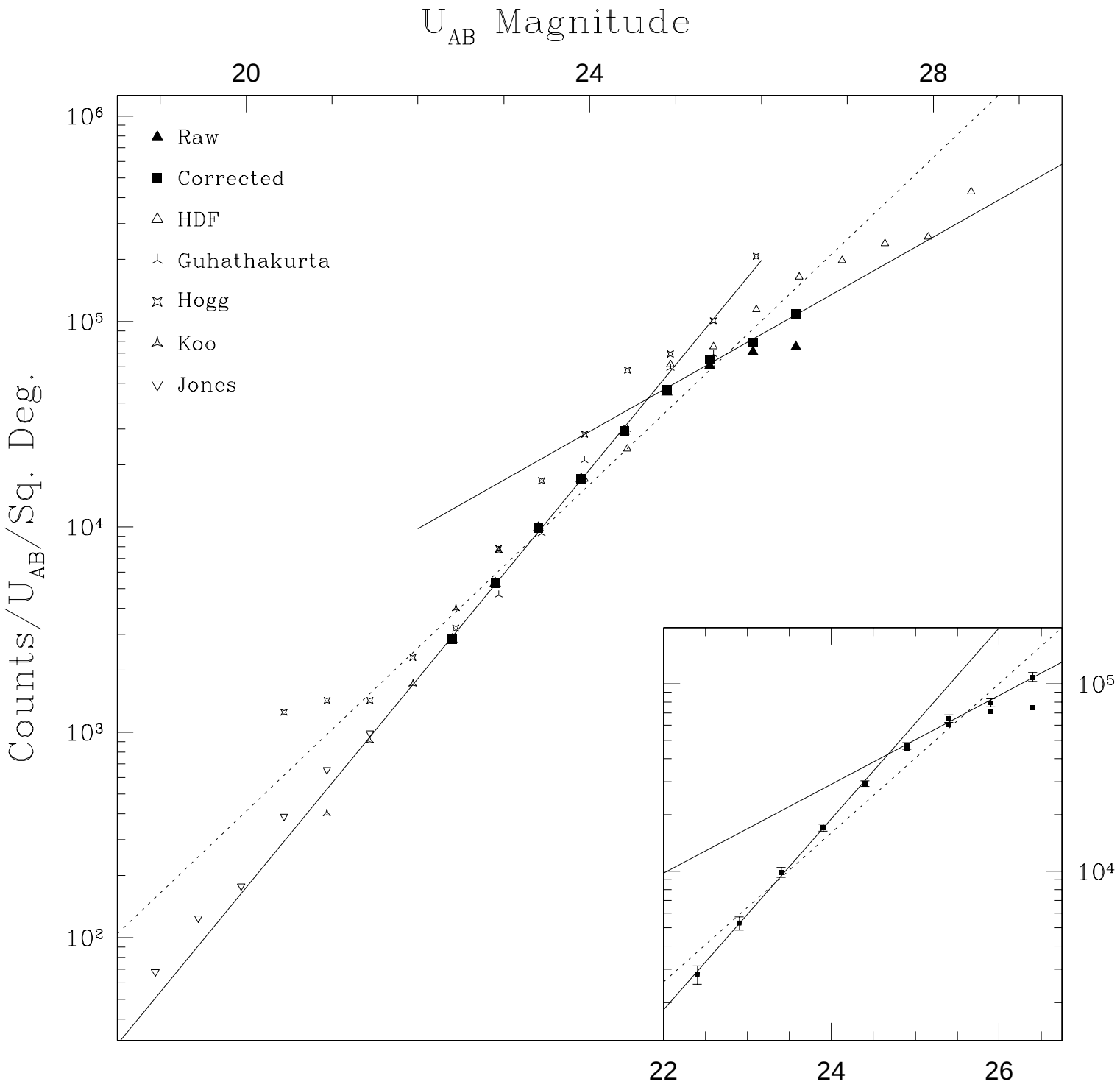
U_{AB} Magnitude
20
24
28
10^6
10^5
10^4
10^3
10^2
Counts/U_{AB}/Sq. Deg.
Raw
Corrected
HDF
Guhathakurta
Hogg
Koo
Jones
22
24
26
10^5
10^4

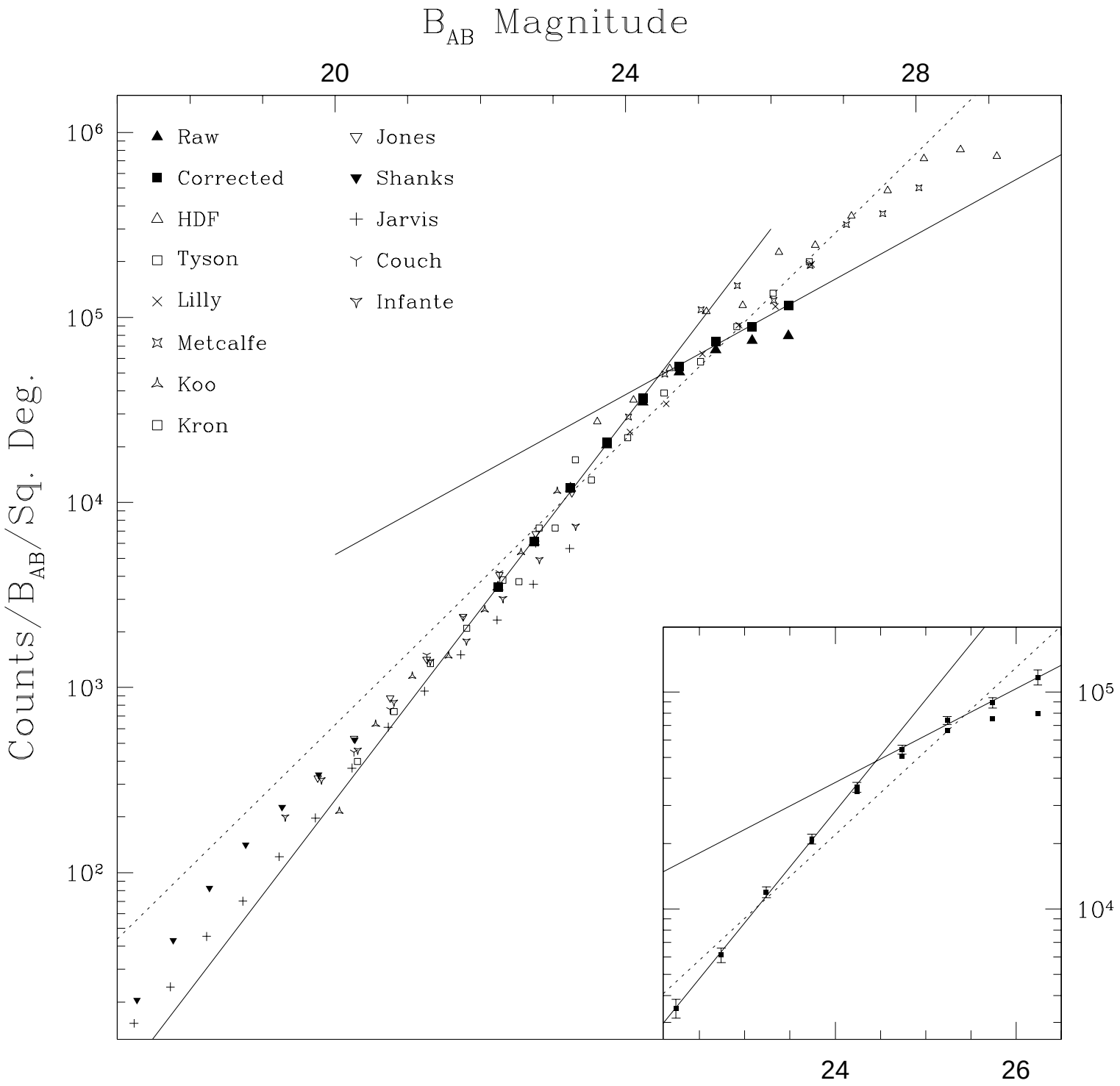
B_{AB} Magnitude
20
24
28
10^6
10^5
10^4
10^3
10^2
Counts/B_{AB}/Sq. Deg.
Raw
Corrected
HDF
Tyson
Lilly
Metcalfe
Koo
Kron
Jones
Shanks
Jarvis
Couch
Infante
10^5
10^4
24
26

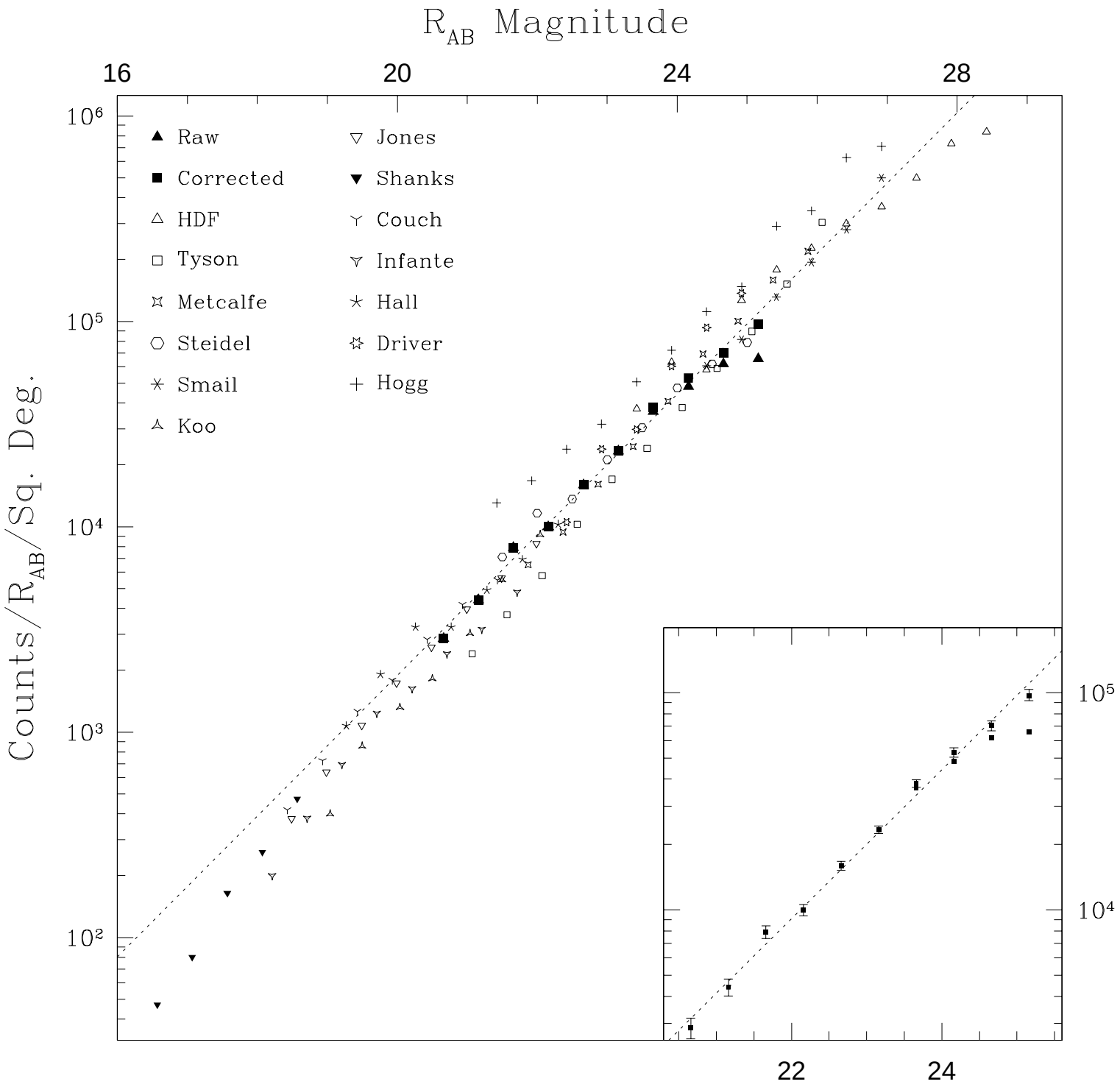
R_{AB} Magnitude
16
20
24
28
10^6
10^5
10^4
10^3
10^2
Counts/R_{AB}/Sq. Deg.
Raw
Corrected
HDF
Tyson
Metcalfe
Steidel
Smail
Koo
Jones
Shanks
Couch
Infante
Hall
Driver
Hogg
10^5
10^4
22
24

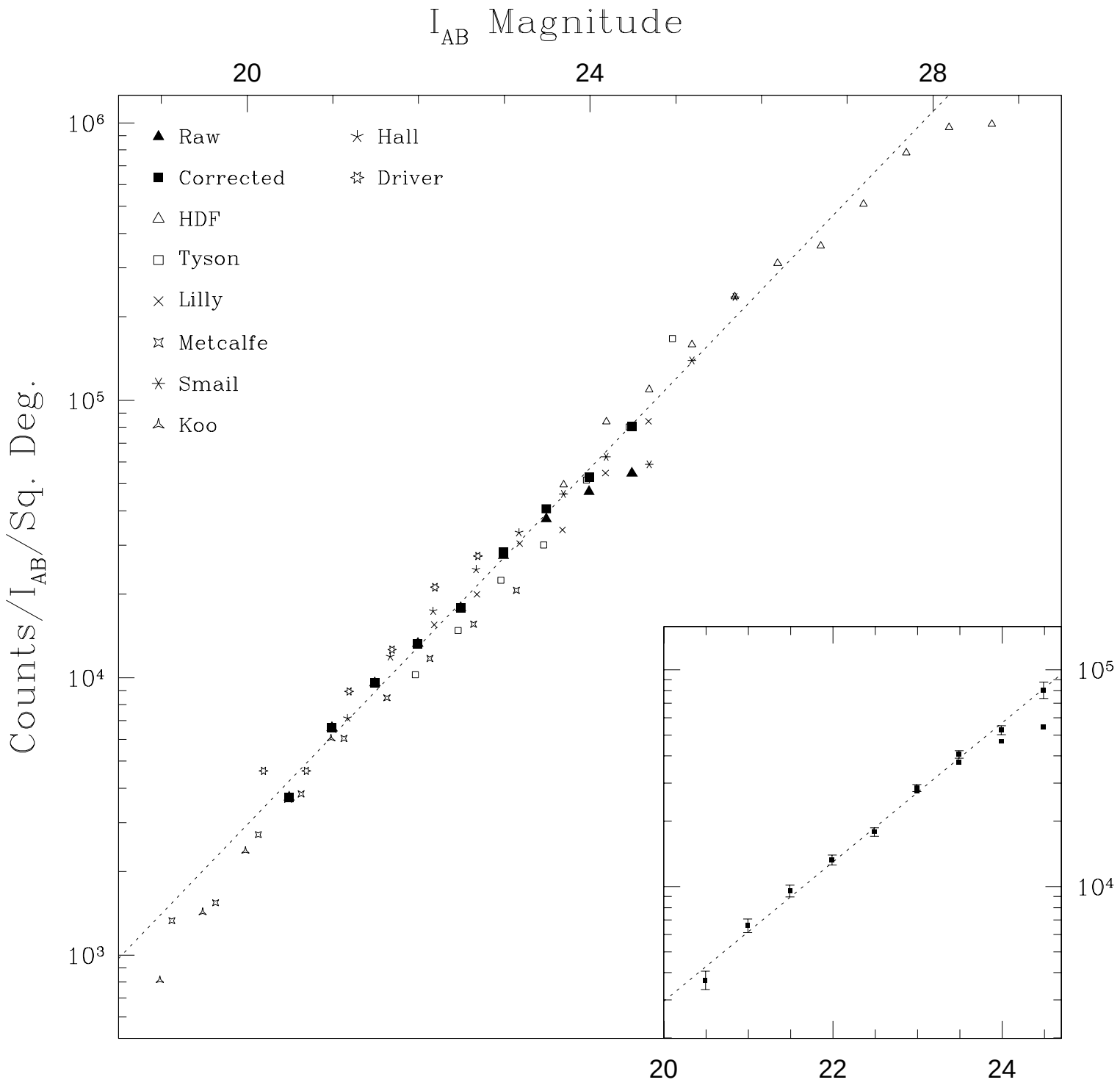
I_{AB} Magnitude
20
24
28
10^6
10^5
10^4
10^3
Counts/I_{AB}/Sq. Deg.
Raw
Corrected
HDF
Tyson
Lilly
Metcalfe
Smail
Koo
Hall
Driver
20
22
24
10^5
10^4

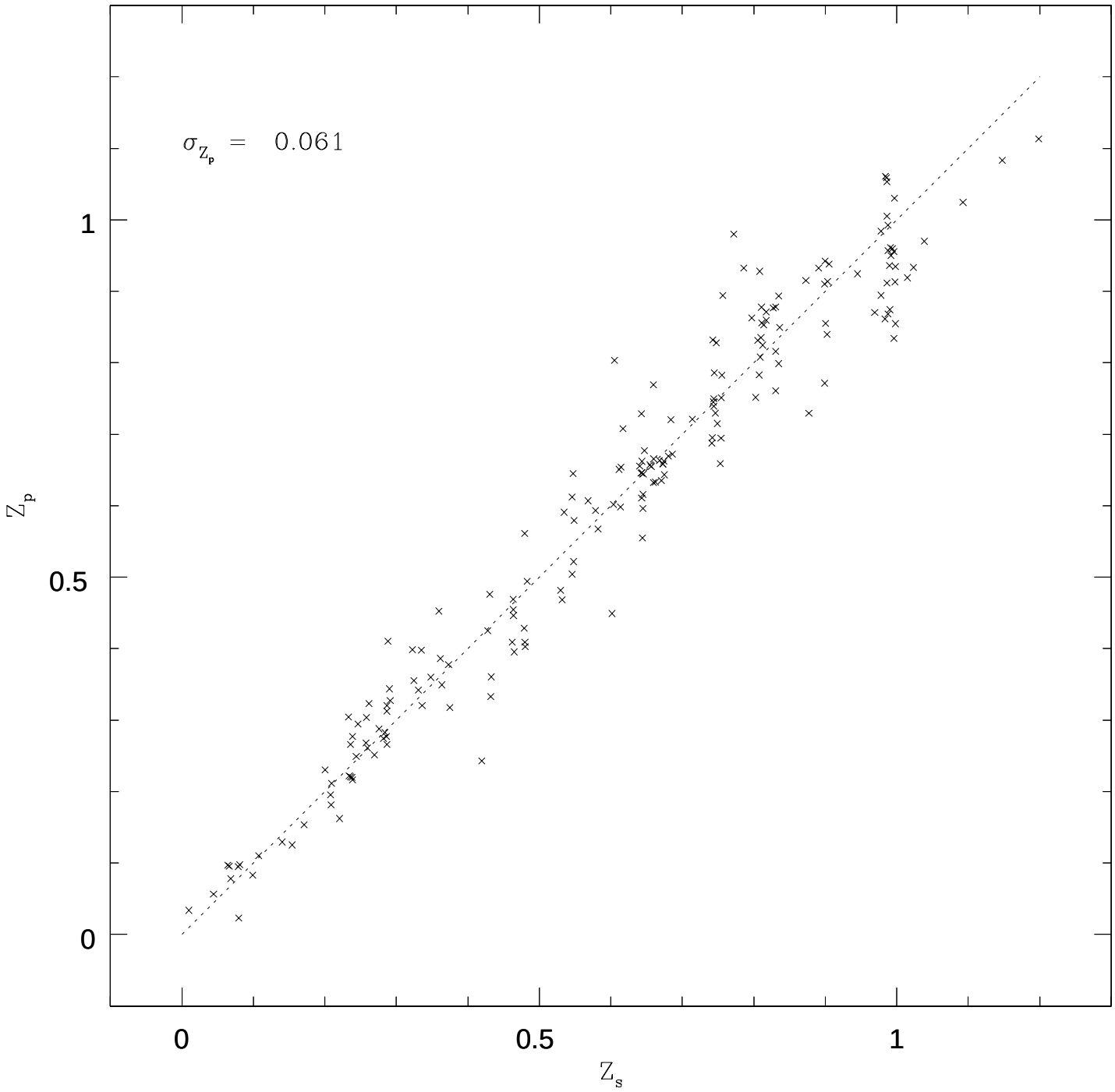
σ_{Z_p} = 0.061
1
0.5
0
Z_p
0
0.5
1
Z_s

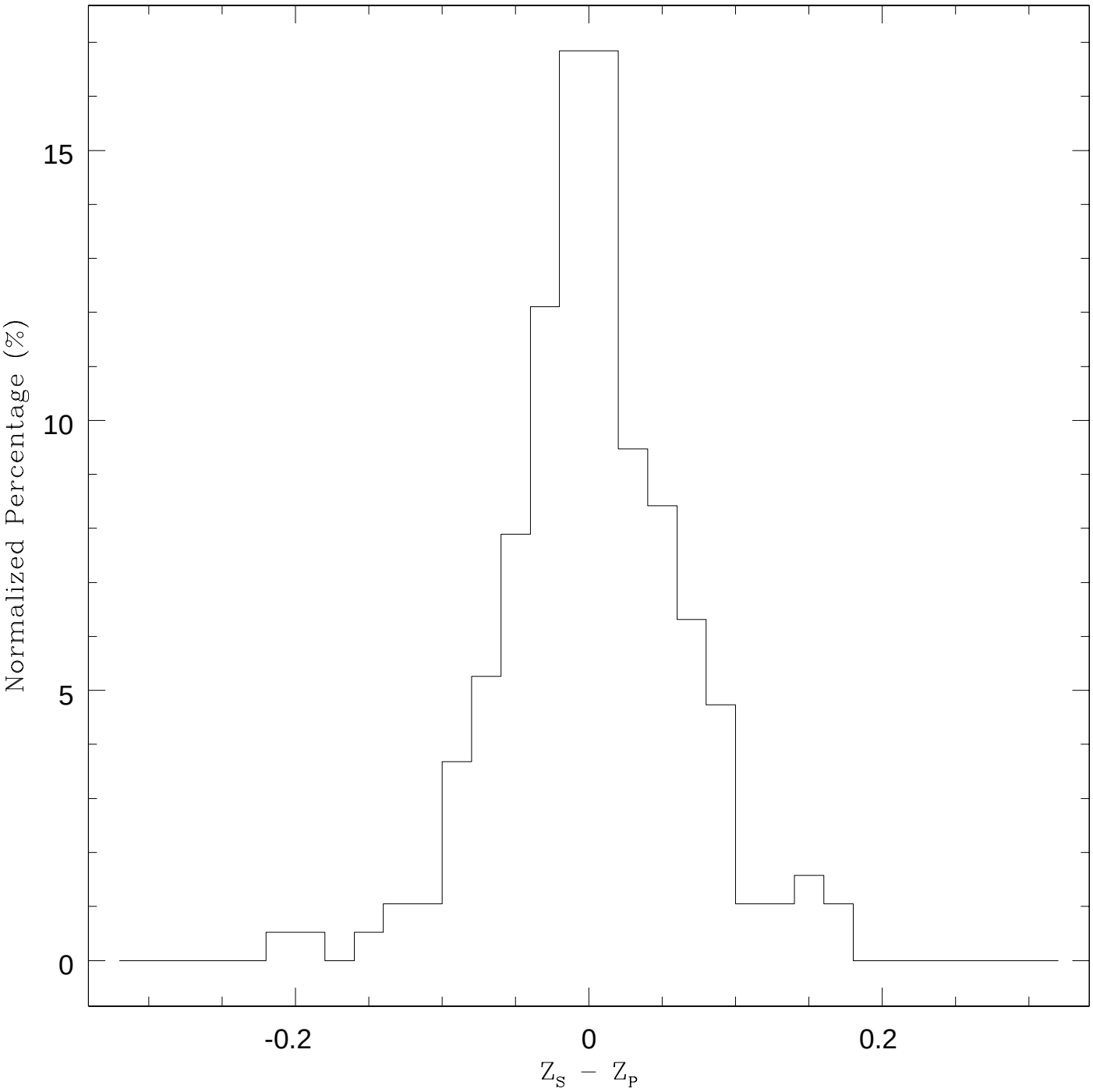
Normalized Percentage (%)
15
10
5
0
-0.2
0
0.2
$Z_S - Z_P$

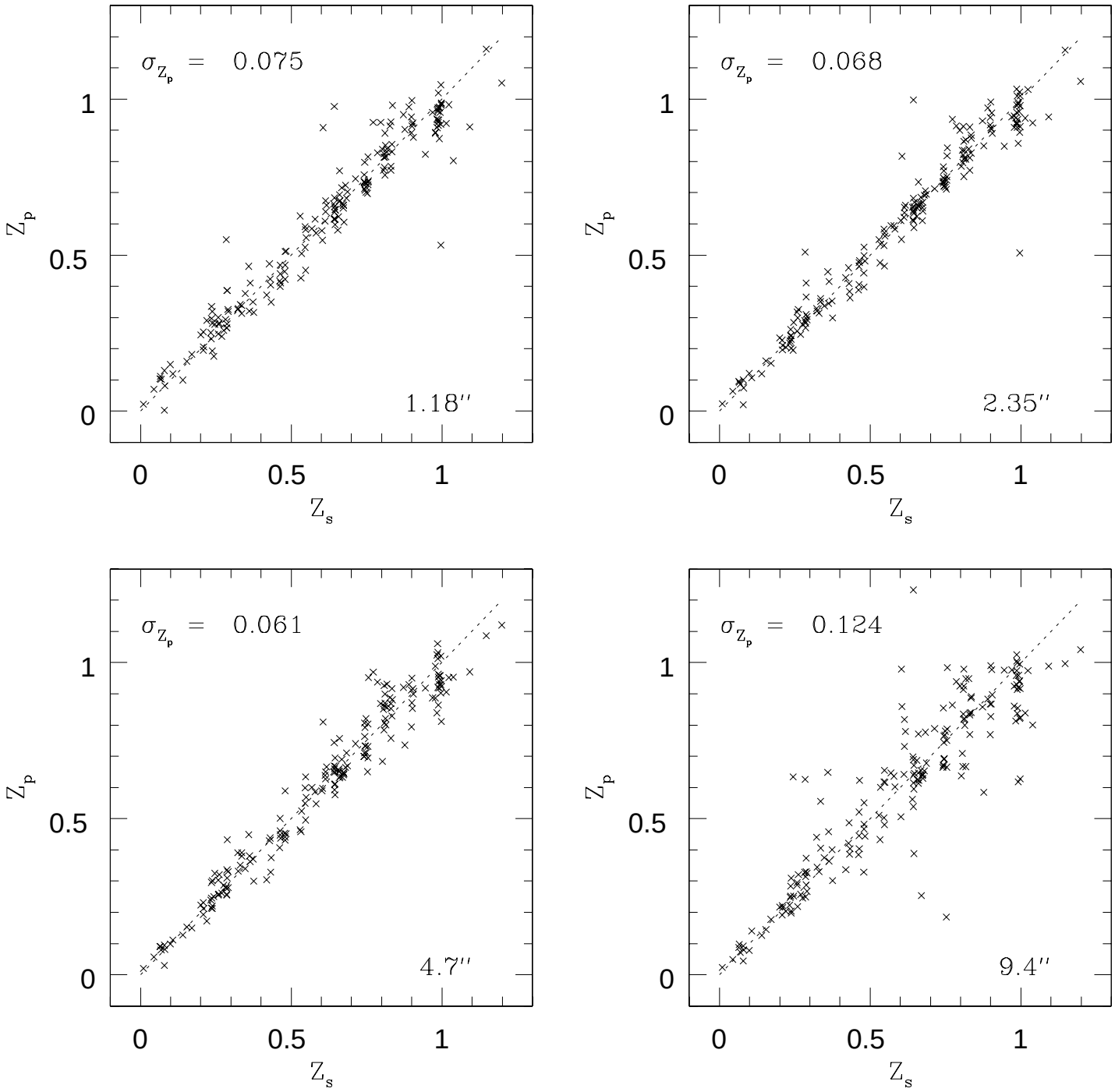
σ_{Z_p} = 0.075
1.18″
σ_{Z_p} = 0.068
2.35″
σ_{Z_p} = 0.061
4.7″
σ_{Z_p} = 0.124
9.4″
Z_p
Z_s
0
0.5
1

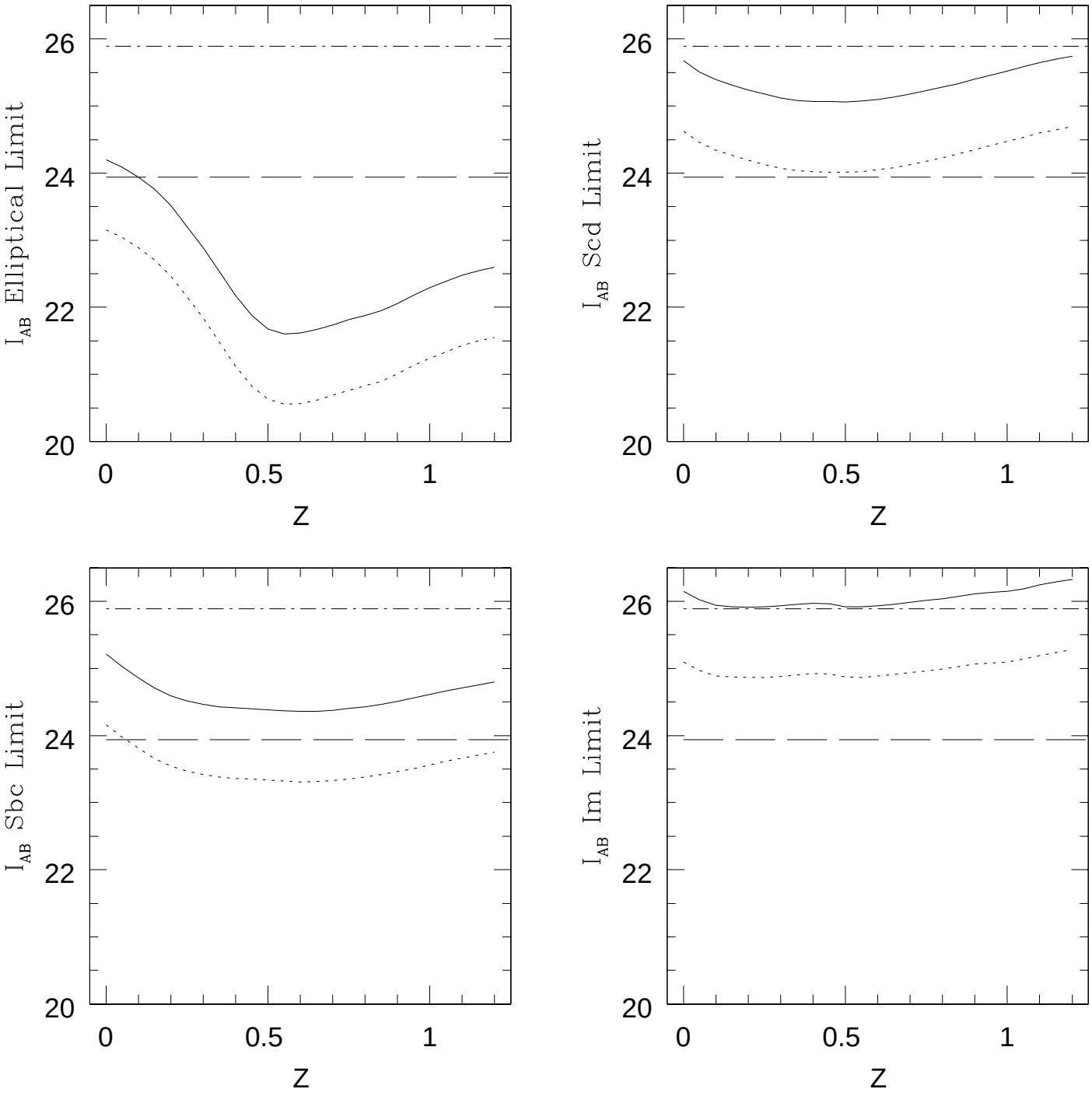
I_{AB} Elliptical Limit
I_{AB} Scd Limit
I_{AB} Sbc Limit
I_{AB} Im Limit
26
24
22
20
0
0.5
1
Z

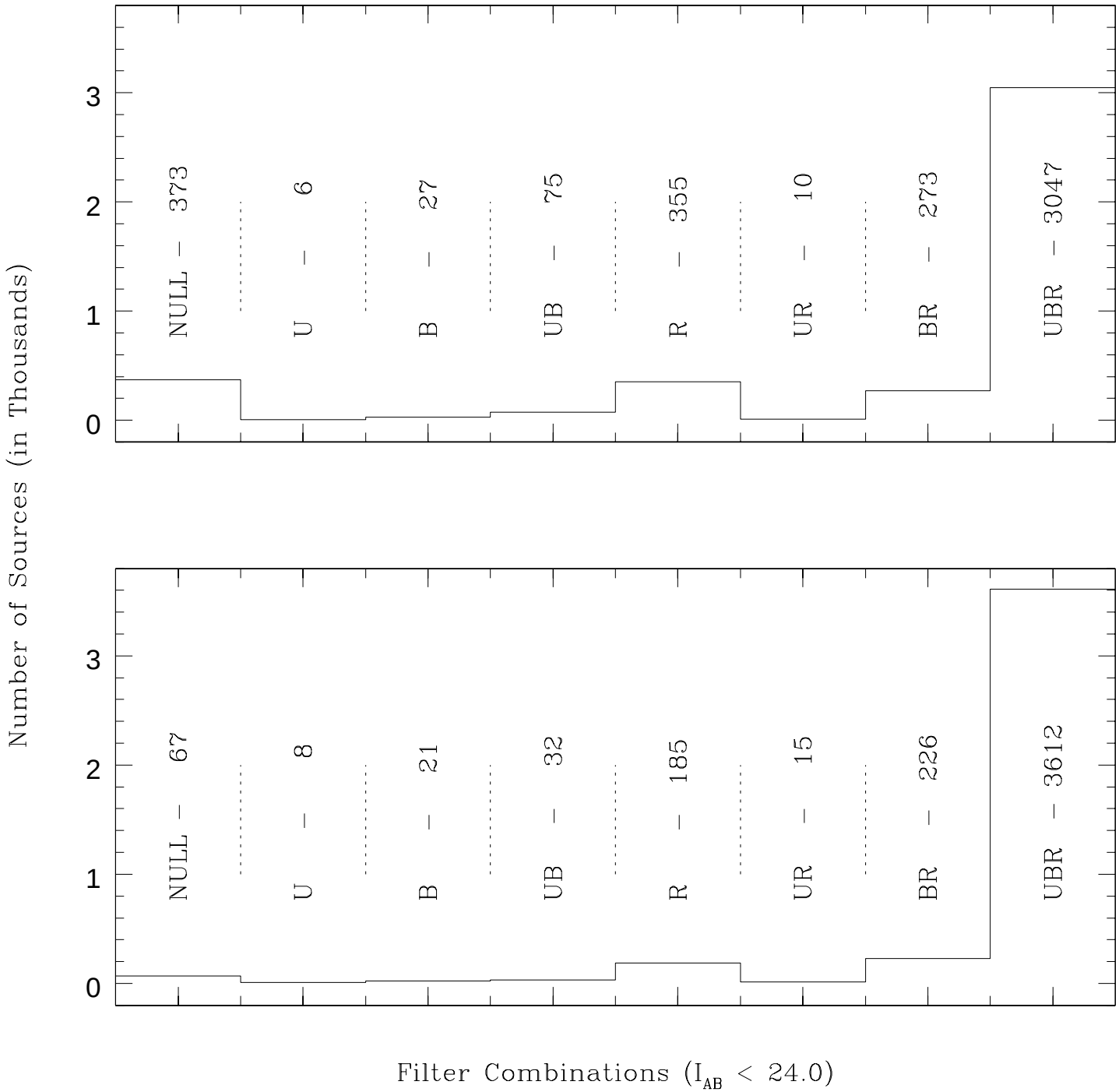
Number of Sources (in Thousands)
0
1
2
3
NULL – 373
U – 6
B – 27
UB – 75
R – 355
UR – 10
BR – 273
UBR – 3047
NULL – 67
U – 8
B – 21
UB – 32
R – 185
UR – 15
BR – 226
UBR – 3612
Filter Combinations (I_{AB} < 24.0)

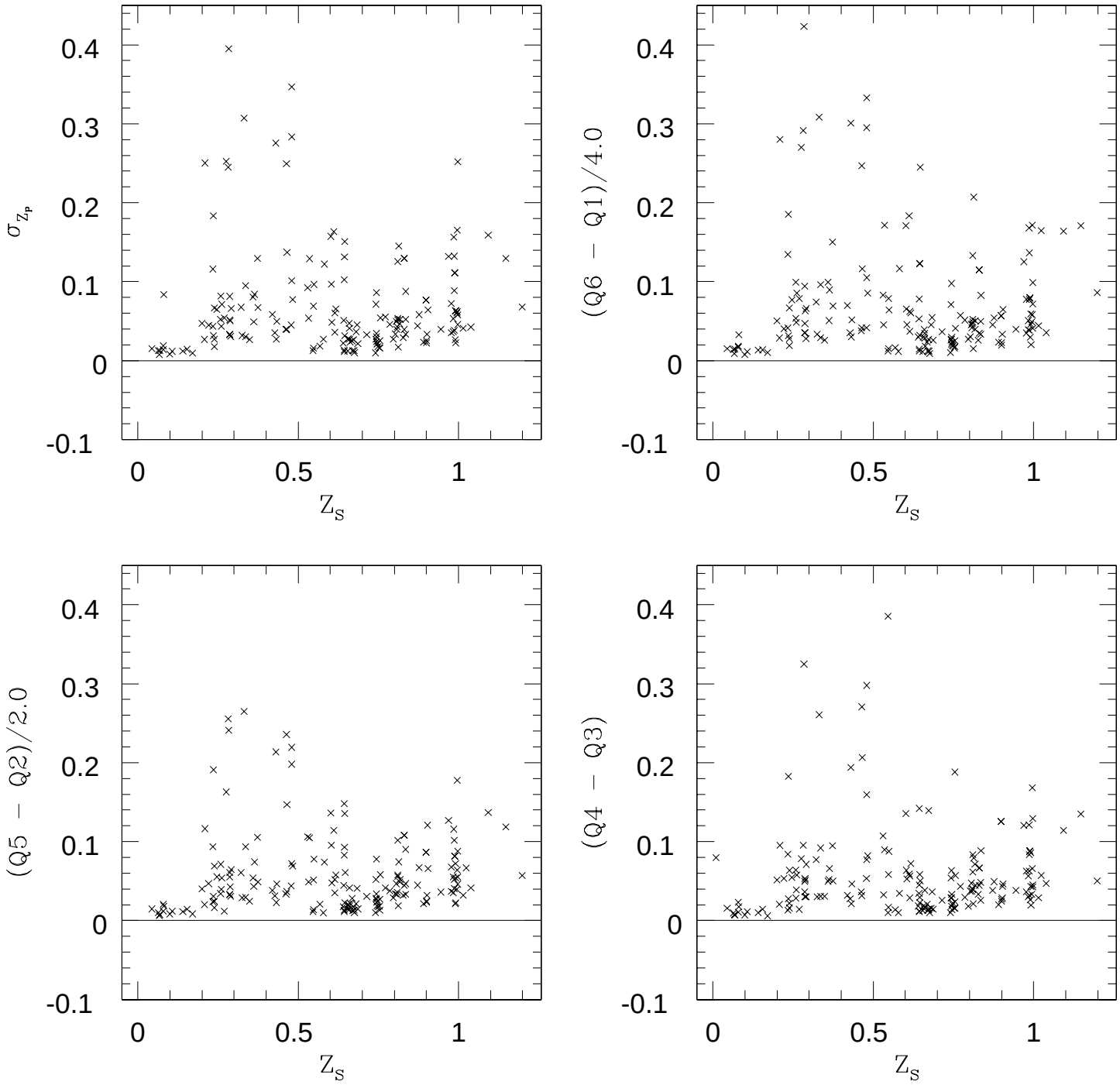
σ_{Z_P}
Z_S
$(Q6 - Q1)/4.0$
Z_S
$(Q5 - Q2)/2.0$
Z_S
$(Q4 - Q3)$
Z_S

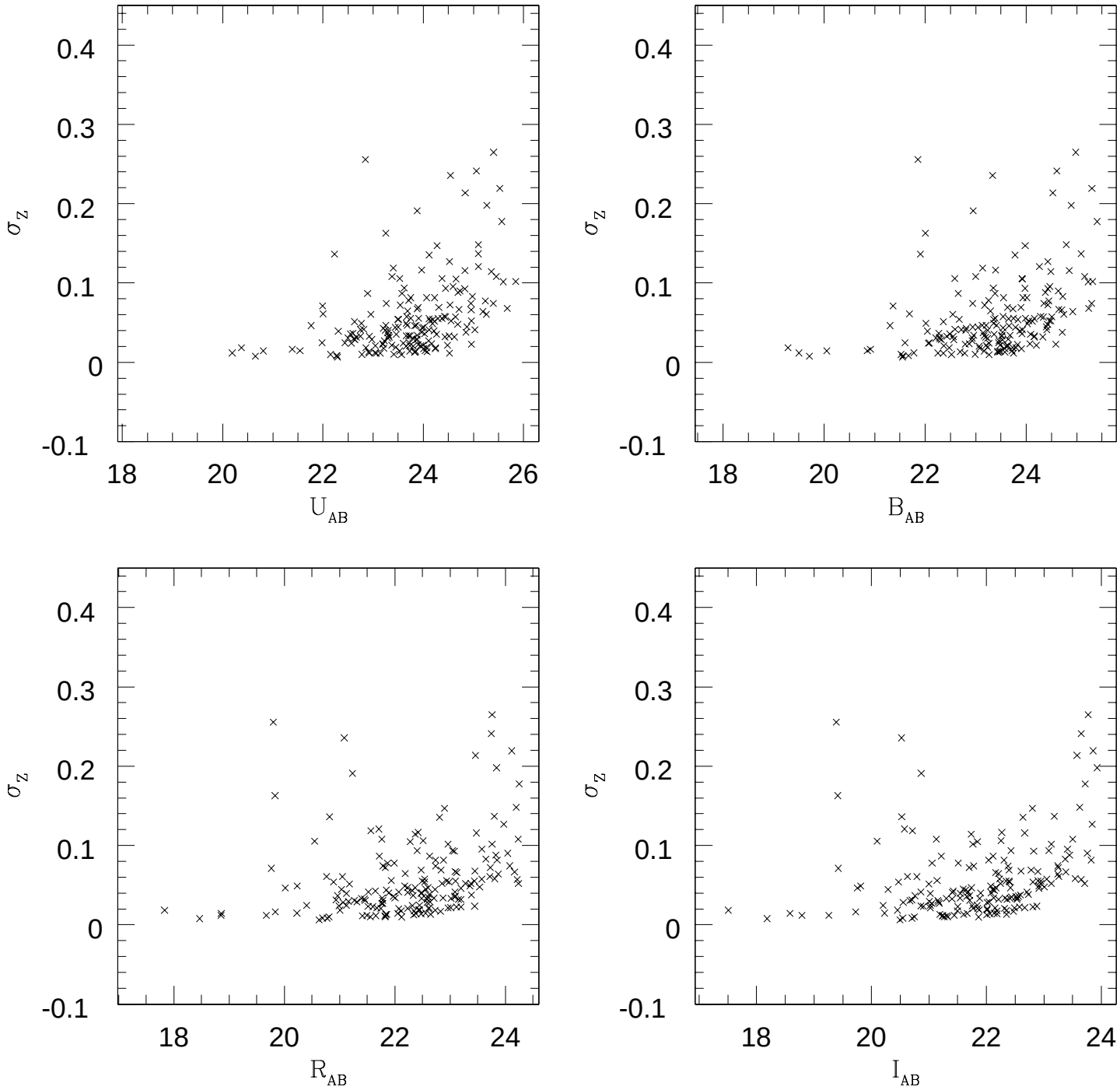
0.4
0.3
0.2
0.1
0
-0.1
σ_z
18
20
22
24
26
U_{AB}
B_{AB}
R_{AB}
I_{AB}

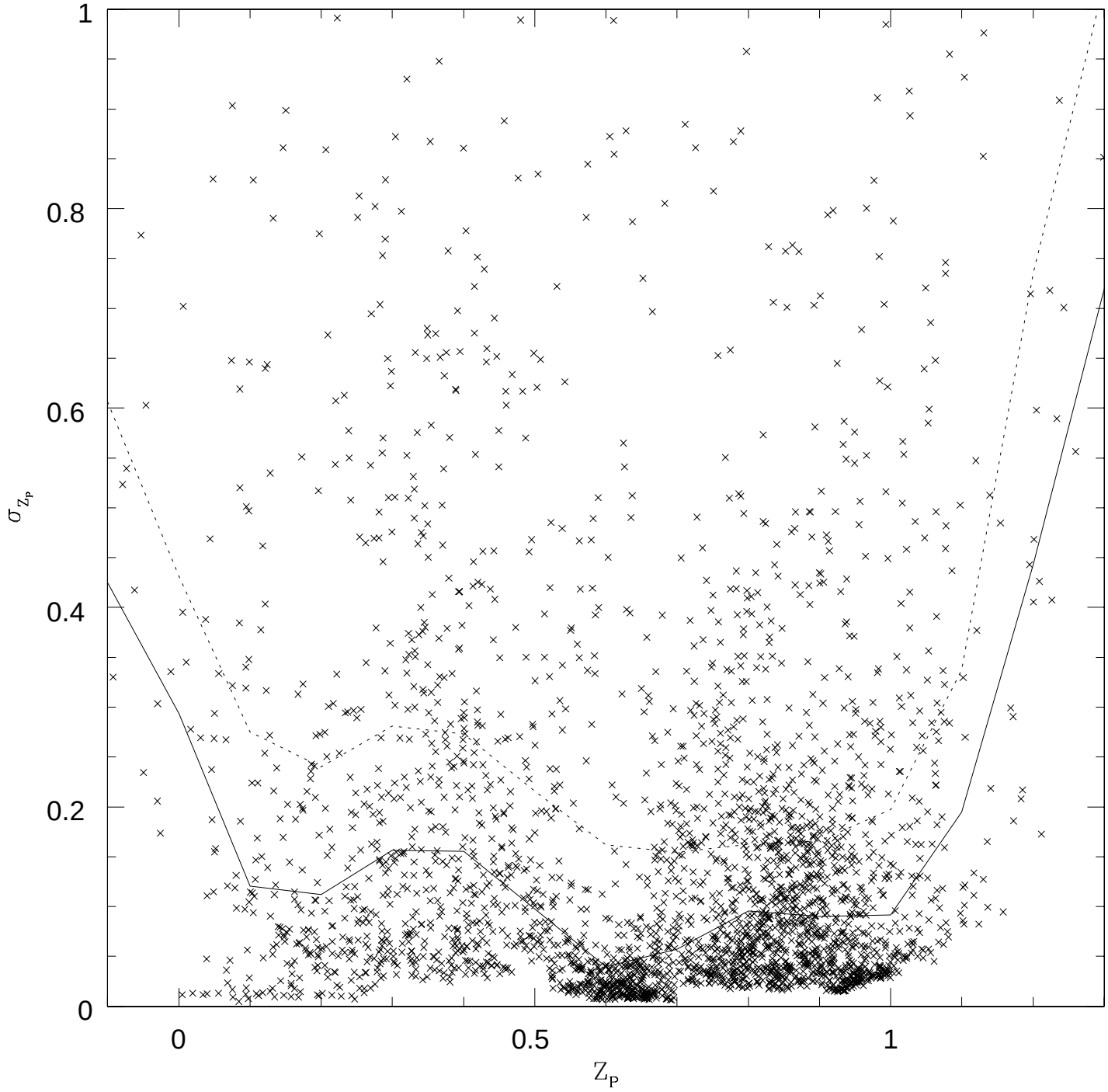
1
0.8
0.6
0.4
0.2
0
σ_{Z_P}
0
0.5
1
Z_P

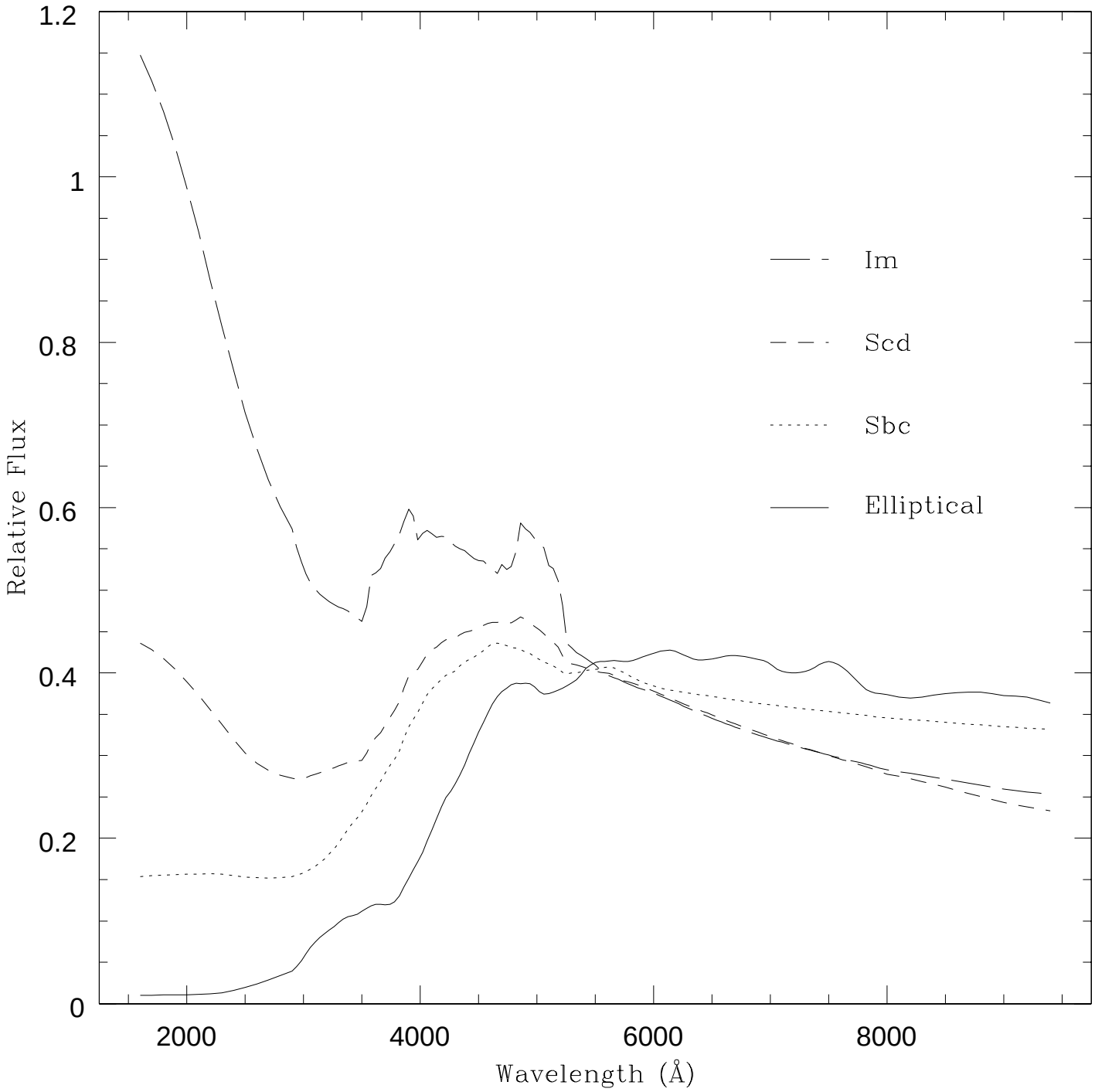
1.2
1
0.8
0.6
0.4
0.2
0
Relative Flux
2000
4000
6000
8000
Wavelength (Å)
Im
Scd
Sbc
Elliptical

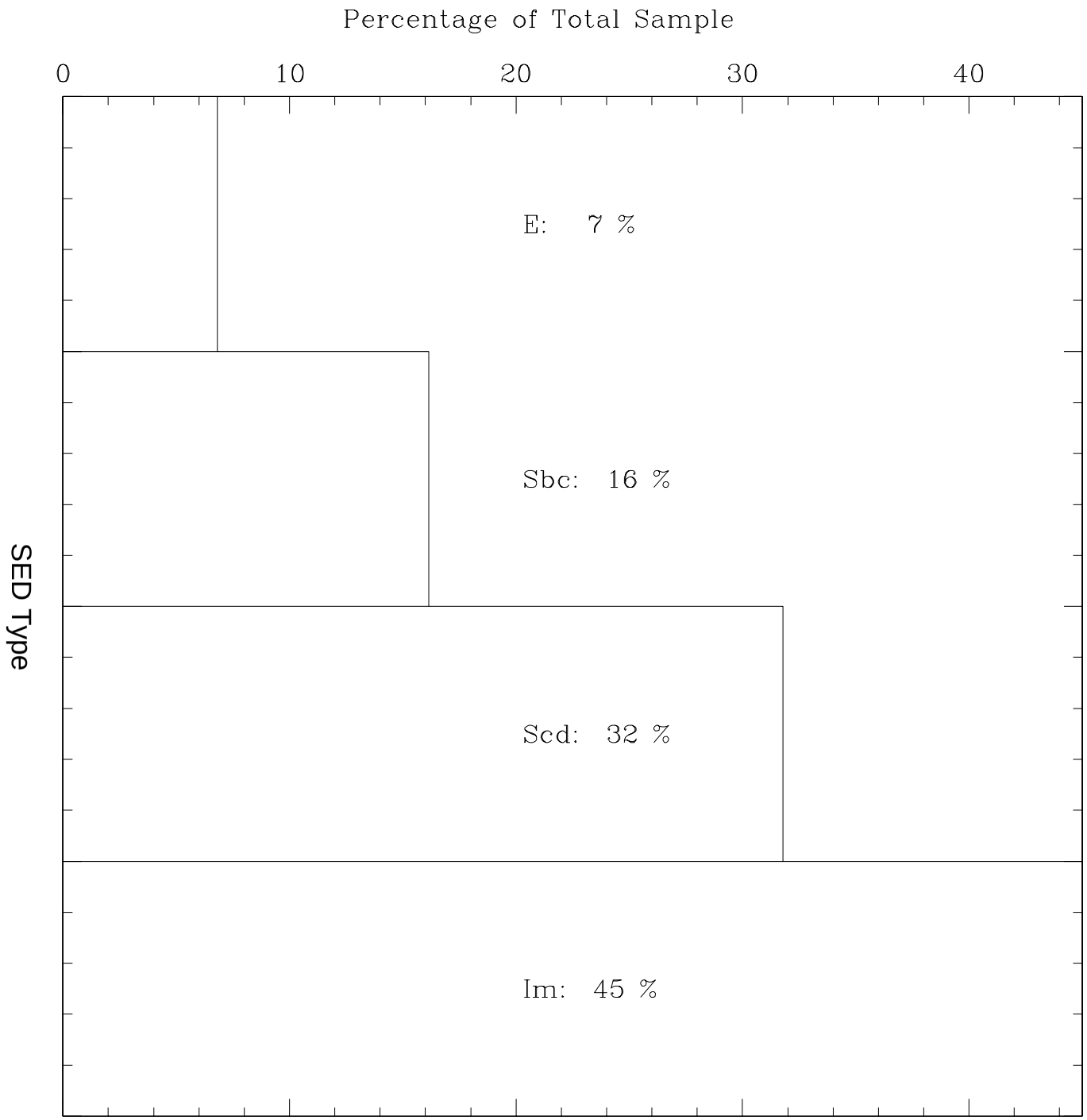
Percentage of Total Sample
0
10
20
30
40
SED Type
E: 7 %
Sbc: 16 %
Scd: 32 %
Im: 45 %

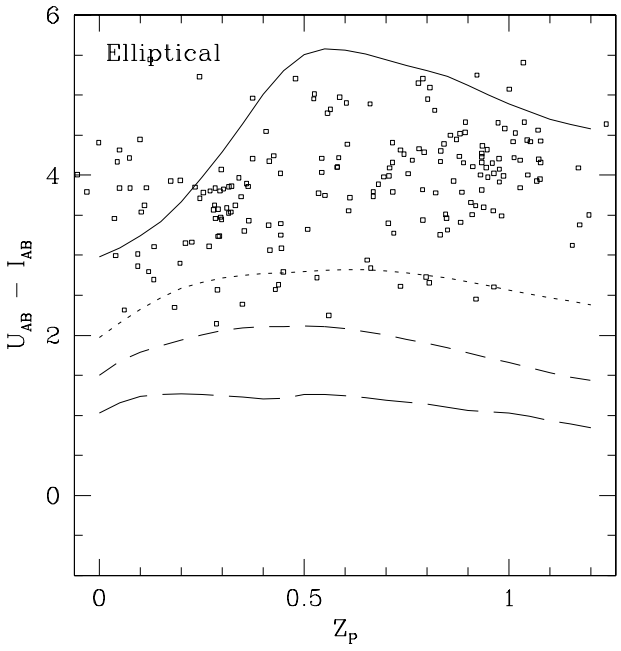
Elliptical
$U_{AB} - I_{AB}$
Z_P
0
2
4
6
0
0.5
1

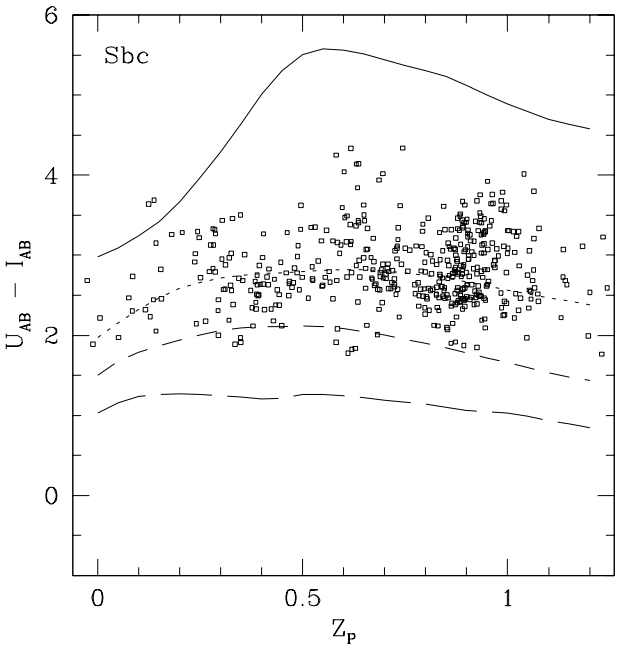
Sbc
$U_{AB} - I_{AB}$
Z_P
0
2
4
6
0
0.5
1

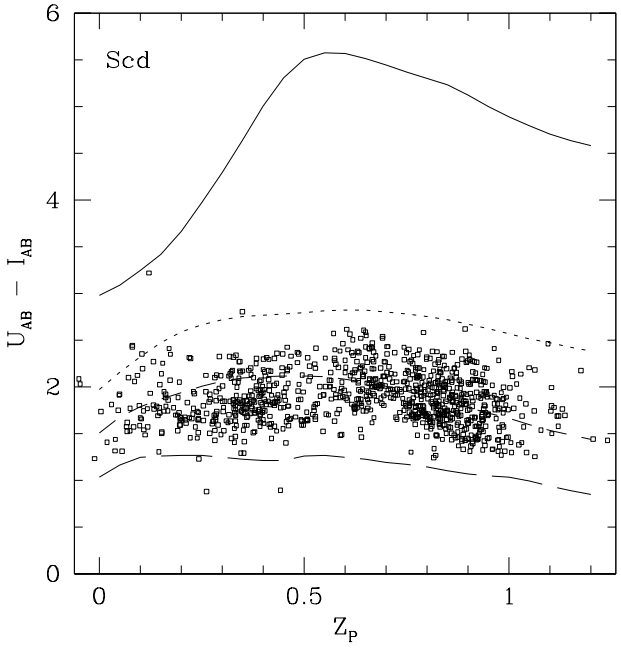
Scd
$U_{AB} - I_{AB}$
Z_P
0
2
4
6
0
0.5
1

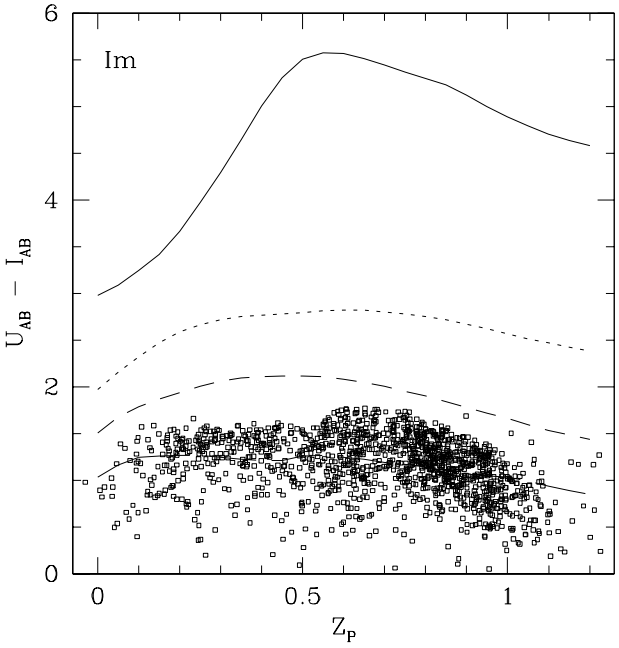
Im
$U_{AB} - I_{AB}$
Z_P
0
2
4
6
0
0.5
1

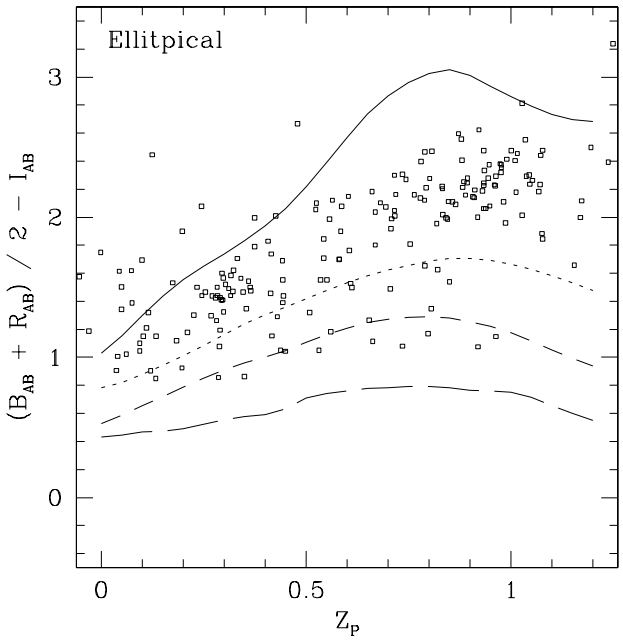
Ellitpical
$(B_{AB} + R_{AB}) / 2 - I_{AB}$
Z_P
0
0.5
1
0
1
2
3

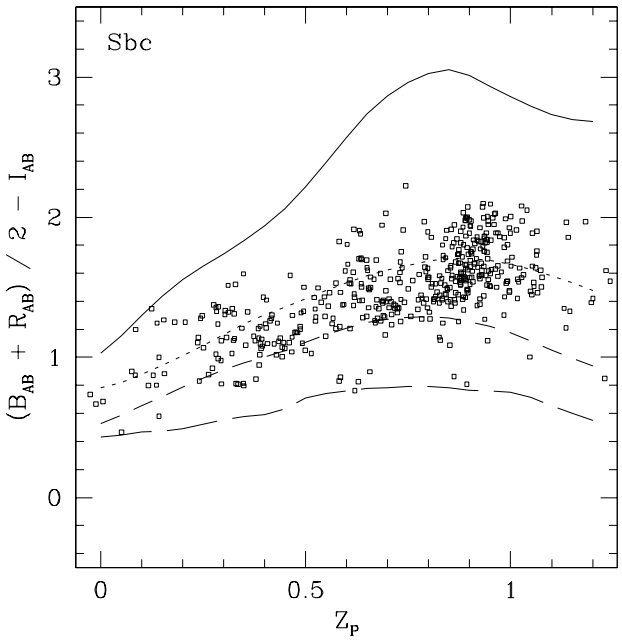
Sbc
$(B_{AB} + R_{AB}) / 2 - I_{AB}$
Z_P
0
0.5
1
0
1
2
3

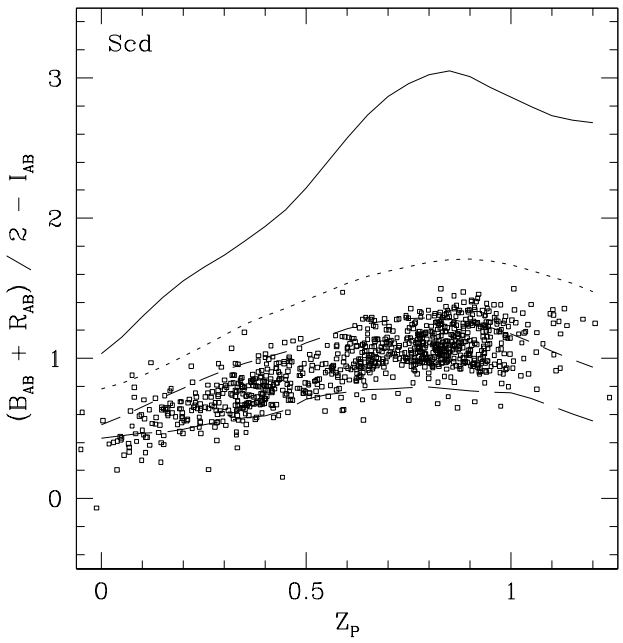
Scd
$(B_{AB} + R_{AB}) / 2 - I_{AB}$
Z_P
0
0.5
1
0
1
2
3

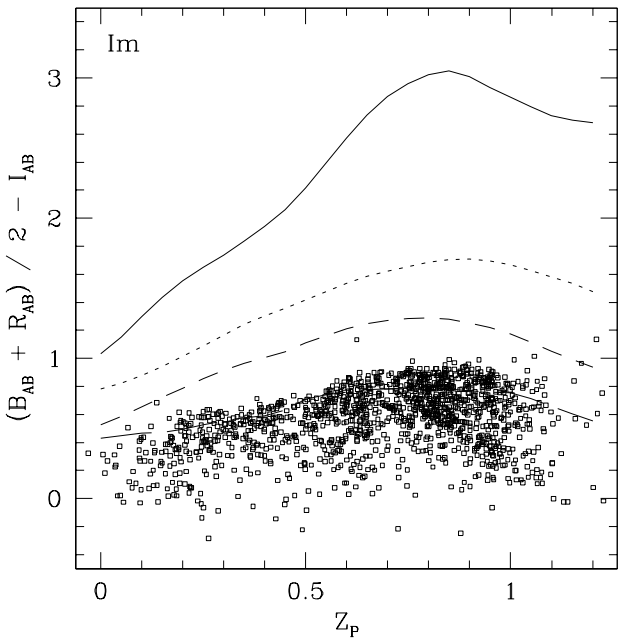
Im
$(B_{AB} + R_{AB}) / 2 - I_{AB}$
Z_P
0
0.5
1
0
1
2
3

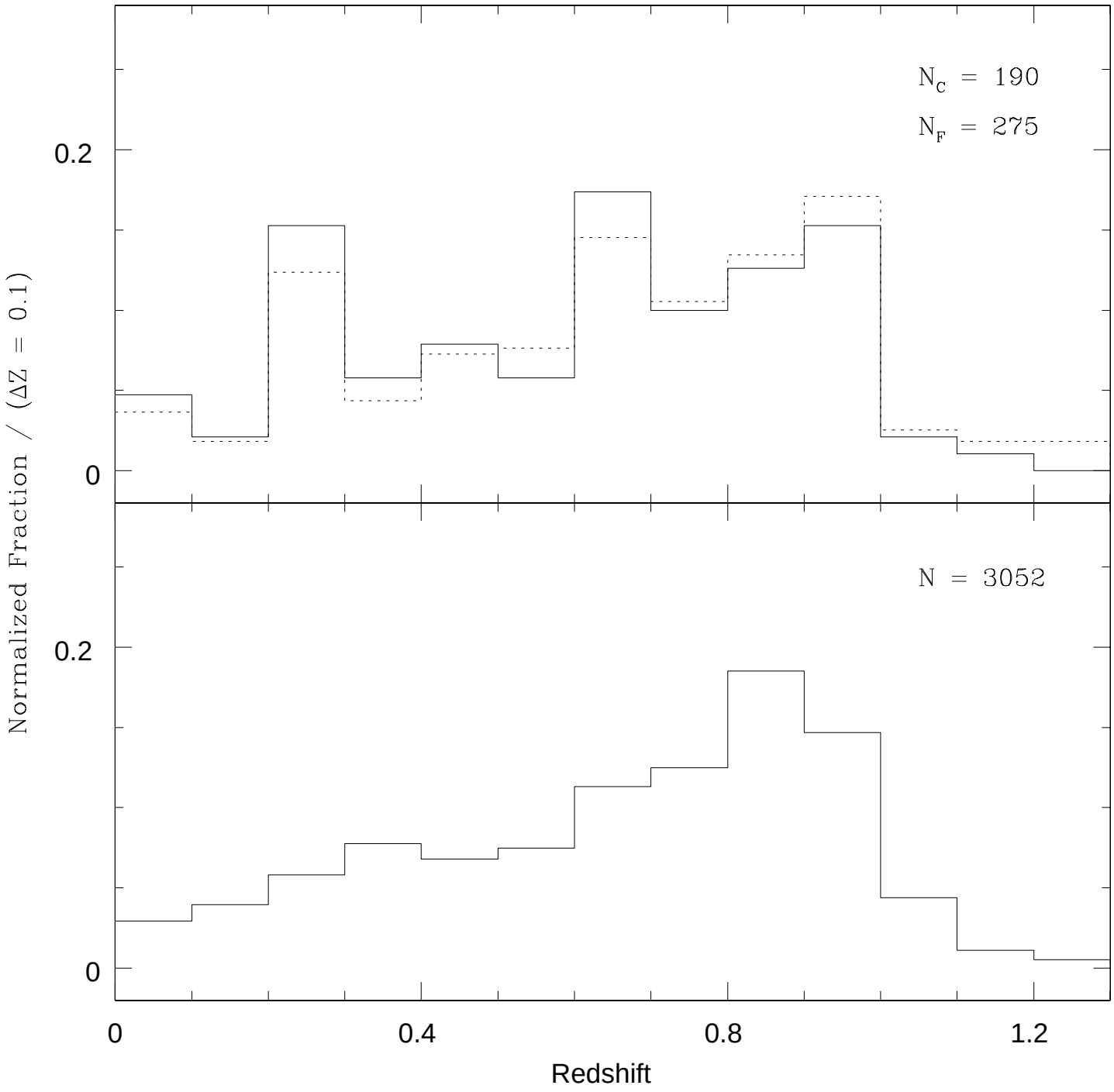
N_C = 190
N_F = 275
N = 3052
0.2
0
0.2
0
0
0.4
0.8
1.2
Redshift
Normalized Fraction / (ΔZ = 0.1)

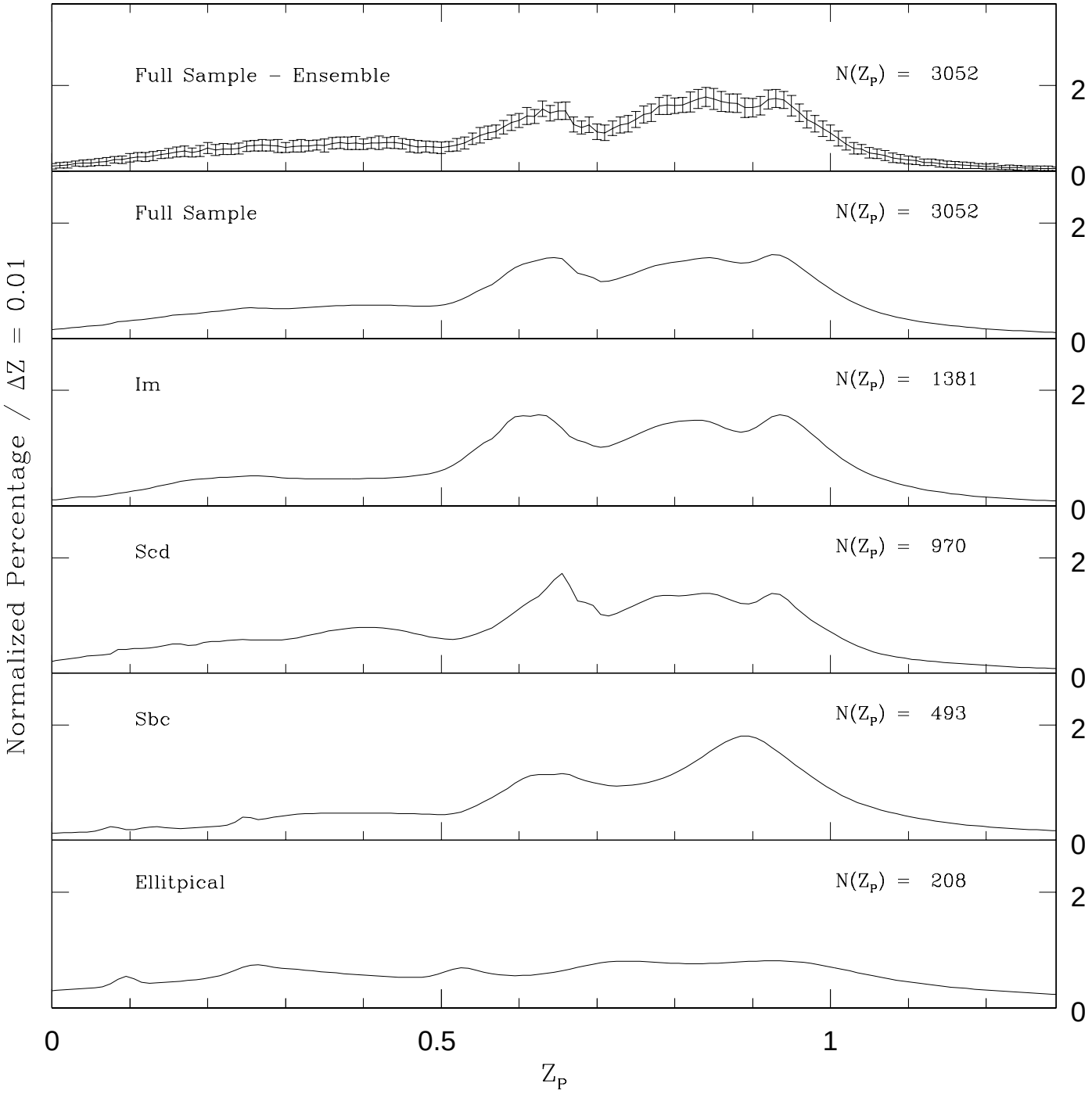
Full Sample – Ensemble
N(Z_P) = 3052
Full Sample
N(Z_P) = 3052
Im
N(Z_P) = 1381
Scd
N(Z_P) = 970
Sbc
N(Z_P) = 493
Ellitpical
N(Z_P) = 208
Normalized Percentage / ΔZ = 0.01
0
2
0.5
1
Z_P